EUROPEAN ORGANISATION FOR NUCLEAR RESEARCH (CERN)

Submitted to: JHEP

CERN-EP-2022-115
4th July 2022

Search for heavy resonances decaying into a Z or W boson and a Higgs boson in final states with leptons and b-jets in 139 fb^{-1} of pp collisions at $\sqrt{s}$ = 13 TeV with the ATLAS detector

The ATLAS Collaboration

This article presents a search for new resonances decaying into a Z or W boson and a 125 GeV Higgs boson h, and it targets the $\nu\bar{\nu}b\bar{b}$, $\ell^+\ell^-b\bar{b}$, or $\ell^\pm\nu b\bar{b}$ final states, where $\ell = e$ or μ, in proton–proton collisions at $\sqrt{s}$ =13 TeV. The data used correspond to a total integrated luminosity of 139 fb^{-1} collected by the ATLAS detector during Run 2 of the LHC at CERN. The search is conducted by examining the reconstructed invariant or transverse mass distributions of Zh or Wh candidates for evidence of a localised excess in the mass range from 220 GeV to 5 TeV. No significant excess is observed and 95% confidence-level upper limits between 1.3 pb, and 0.3 fb are placed on the production cross section times branching fraction of neutral and charged spin-1 resonances and CP-odd scalar bosons. These limits are converted into constraints on the parameter space of the Heavy Vector Triplet model and the two-Higgs-doublet model.

1 Introduction

Following the discovery of the Higgs boson [1, 2] by the ATLAS and CMS collaborations at the Large Hadron Collider (LHC), measurements of its properties so far indicate consistency with the Standard Model (SM) predictions. Nevertheless, several questions related to electroweak symmetry breaking remain open, in particular how the Higgs boson mass is protected against large radiative corrections (the naturalness problem [3–5]) and whether the Higgs boson is part of an extended scalar sector.

Various models with dynamical electroweak symmetry breaking scenarios attempt to solve the naturalness problem by assuming new strong interactions at a higher energy scale. These models generally predict the existence of new vector resonances that have significant branching fractions for decays into a vector boson and a Higgs boson. Examples are Minimal Walking Technicolour [6–8], Little Higgs [9], or composite Higgs models [10, 11]. Resonance searches are typically not sensitive to all free parameters of the underlying theory, so simplified models are generally used, such as the Heavy Vector Triplet (HVT) parameterised Lagrangian [12, 13], which adds an additional SU(2) field to the SM and provides a restricted number of new couplings.

A second class of models extend the scalar sector by including additional Higgs singlets or doublets [14]. Examples of models with an extended scalar sector are the minimal supersymmetric SM [15–19], axion models [20], or baryogenesis models [21]. Again, instead of targeting any of these specific theories, a generic two-Higgs-doublet model (2HDM) with a CP-conserving Higgs potential is probed. The scalar sector of the theory consists of five Higgs bosons: two charged ($H^{\pm}$), two neutral CP-even (h, H), and one neutral CP-odd (A).

In this article, ATLAS presents a search for new heavy resonances decaying into a SM Higgs boson h and a Z or W boson in 139 fb^{-1} of proton–proton (pp) collision data at $\sqrt{s}$ =13 TeV. These resonances are assumed to be either a new heavy vector boson, denoted hereafter by Z' and W', or a heavy CP-odd scalar boson A. The article targets leptonic decays of the Z and W bosons, and requires b-quark pair decays for the Higgs boson. Therefore, the search is performed in the following three final states: $\nu\bar{\nu}b\bar{b}$, $\ell^{\pm}\nu b\bar{b}$ and $\ell^{+}\ell^{-}b\bar{b}$. In this article, ℓ represents e or μ unless otherwise stated.

Searches in the same final states have been performed at $\sqrt{s}$ =13 TeV with an integrated luminosity of 36.1 fb^{-1} by ATLAS [22] and of 137 fb^{-1} by CMS [23, 24]. Results in other final states have also been published: ATLAS has performed a search in the fully hadronic final state [25], based on an integrated luminosity of 139 fb^{-1}, and CMS has published results in the fully hadronic final state [26] and the $\tau^{+}\tau^{-}\ell^{+}\ell^{-}$ final state [27], based on a 35.9 fb^{-1} dataset.

Apart from the significantly larger dataset used here, several improvements have been implemented since the previous ATLAS publication [22], including improved b-tagging, lepton isolation and jet reconstruction, a reoptimisation of the lepton selection in the $\ell^{+}\ell^{-}b\bar{b}$ channel and a new selection based on the missing transverse momentum ($E_{\mathrm{T}}^{\mathrm{miss}}$) significance in the $\nu\bar{\nu}b\bar{b}$ channel (see Sections 4 and 5).

The search presented in this article is performed by seeking a localised excess in the distribution of a channel-dependent proxy for the resonance mass of the $\nu\bar{\nu}b\bar{b}$, $\ell^{\pm}\nu b\bar{b}$ and $\ell^{+}\ell^{-}b\bar{b}$ systems. Signal mass hypotheses in a range from 220 GeV to 5 TeV are tested. Due to the wide range of probed Higgs boson transverse momenta, two methods are used to reconstruct Higgs boson candidates. At low transverse momenta, the decay products of the Higgs boson are reconstructed as individual jets, while at high transverse momenta they are reconstructed as a single large-radius jet.

The search selects events in signal regions (SR) and background-dominated control regions (CR) based on requirements placed on kinematic properties of final-state particles and on event-level quantities. The statistical interpretation is performed with a binned maximum-likelihood fit to data based on the reconstructed resonance mass, using the signal and control regions. The major backgrounds are modelled using simulation and their normalisations are determined by the fit. Different fit models are used depending on the targeted signal hypothesis, production mode, or final state.

The results of the HVT Z' and W' searches are interpreted in two benchmark models. In the first model, referred to as *Model A*, the branching fractions to fermions and gauge bosons are comparable, as in some models with an extended gauge symmetry [28]. For *Model B*, fermionic couplings are suppressed, as in strong dynamical models such as the minimal composite Higgs model [29]. Constraints are also set on the coupling-strength scale factors g_{F} and g_{H}, which modulate the coupling of the Z' and W' bosons to fermions and the Higgs and gauge bosons, respectively. The search focuses on high resonance masses, ranging from 300 GeV to 5 TeV.

The search for $A \to Zh$ focuses on smaller masses, ranging from 220 GeV to 2 TeV, because the Higgs potential becomes unstable for sufficiently large A boson masses in the class of models targeted by this article. The results of the $A \to Zh$ search are interpreted as constraints on the ratio of the vacuum expectation values of the two Higgs doublets, $\tan\beta$, and on $\cos(\beta-\alpha)$, where α is the mixing angle between the two CP-even Higgs bosons, for Type I, Type II, Lepton-specific, and Flipped 2HDMs. These models differ with respect to which doublets couple to the up-type and down-type quarks and to the charged leptons [14]. Production via gluon–gluon fusion (ggA) and production with associated b-quarks ($b\bar{b}A$) are both considered in this search.

Representative lowest-order Feynman diagrams of the relevant production modes[1] for Z', W', and A bosons in pp collisions and the subsequent decays into the $\nu\bar{\nu}b\bar{b}$, $\ell^+\ell^- b\bar{b}$, and $\ell^\pm \nu b\bar{b}$ final states are depicted in Figure 1.

This article is structured as follows. Sections 2 and 3 provide a brief description of the ATLAS experiment and of the data and simulated event samples, respectively. The event reconstruction and selections are discussed in Sections 4 and 5. The background estimation and systematic uncertainties are described in Sections 6 and 7, respectively. Finally, Sections 8 and 9 detail the statistical analysis and then provide a discussion of the results and concluding remarks.

2 ATLAS detector

The ATLAS experiment [30] at the LHC is a multipurpose particle detector with a forward–backward symmetric cylindrical geometry and a near 4π coverage in solid angle.[2] It consists of an inner tracking detector (ID) surrounded by a thin superconducting solenoid providing a 2 T axial magnetic field, electromagnetic and hadron calorimeters, and a muon spectrometer. The inner tracking detector covers

[1] In the HVT benchmark *Models A* and *B*, the Z' and W' bosons are produced mainly via quark–antiquark annihilation, while production via vector-boson fusion is relevant only for the fermiophobic scenario (i.e. *Model C*).

[2] ATLAS uses a right-handed coordinate system with its origin at the nominal interaction point (IP) in the centre of the detector and the z-axis along the beam pipe. The x-axis points from the IP to the centre of the LHC ring, and the y-axis points upwards. Cylindrical coordinates (r,ϕ) are used in the transverse plane, ϕ being the azimuthal angle around the z-axis. The pseudorapidity is defined in terms of the polar angle θ as $\eta = -\ln\tan(\theta/2)$. Angular distance is measured in units of $\Delta R \equiv \sqrt{(\Delta\eta)^2 + (\Delta\phi)^2}$.

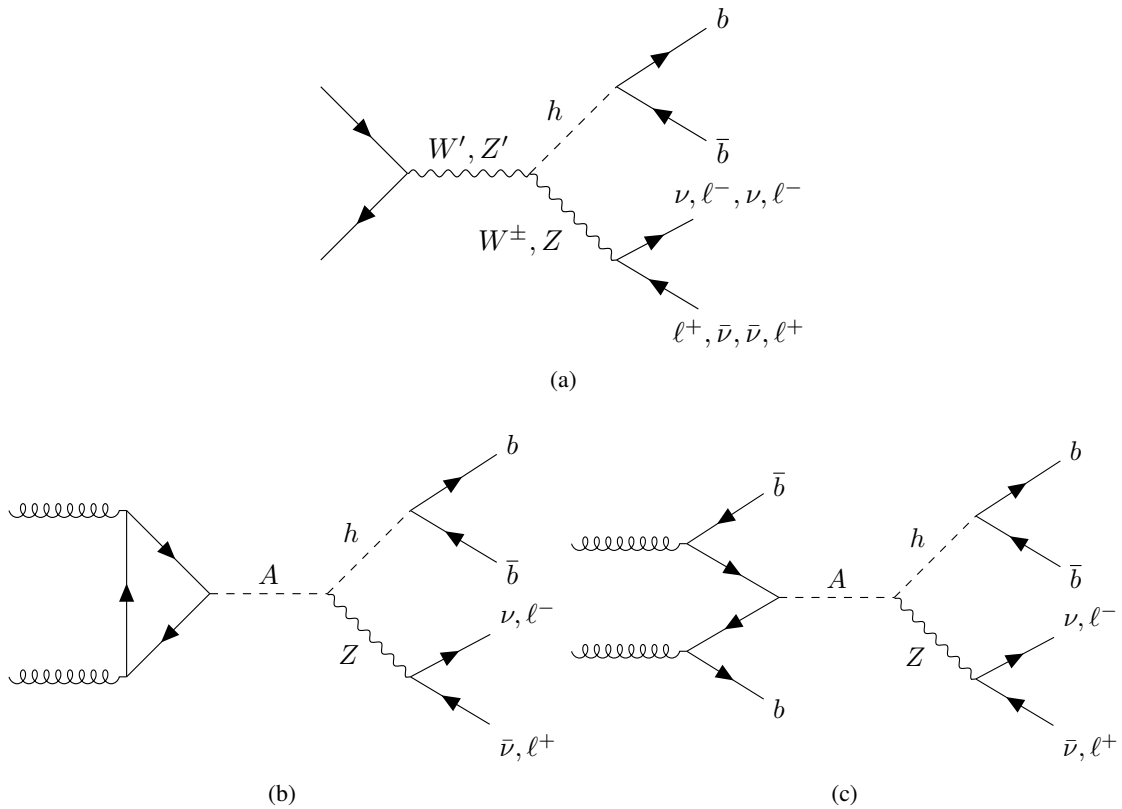

Figure 1: Representative lowest-order Feynman diagrams of the resonant production of a W or Z boson and a Higgs boson via (a) quark–antiquark annihilation, (b) gluon–gluon fusion and (c) b-associated production. The subsequent decays into the $\nu\bar{\nu}b\bar{b}$, $\ell^{\pm}\nu b\bar{b}$ and $\ell^{+}\ell^{-}b\bar{b}$ final states are also depicted, where $\ell = e, \mu$, and τ.

the pseudorapidity range $|\eta| < 2.5$. It consists of silicon pixel, silicon microstrip, and transition radiation tracking detectors. Lead/liquid-argon (LAr) sampling calorimeters provide electromagnetic energy measurements with high granularity. A steel/scintillator-tile hadron calorimeter covers the central pseudorapidity range ($|\eta| < 1.7$). The endcap and forward regions are instrumented with LAr calorimeters for both the electromagnetic and hadronic energy measurements up to $|\eta| = 4.9$. The muon spectrometer surrounds the calorimeters and is based on three large superconducting air-core toroidal magnets with eight coils each. The field integral of the toroids ranges between 2.0 and 6.0 T m across most of the detector. The muon spectrometer includes a system of precision tracking chambers and fast detectors for triggering. A two-level trigger system is used to select events. The first-level trigger is implemented in hardware and uses a subset of the detector information to accept events at a rate below 100 kHz. This is followed by a software-based trigger that reduces the accepted event rate to 1 kHz on average depending on the data-taking conditions. An extensive software suite [31] is used in the reconstruction and analysis of real and simulated data, in detector operations, and in the trigger and data acquisition systems of the experiment.

3 Data and Monte Carlo samples

The data used in this analysis were recorded with the ATLAS detector between 2015 and 2018 in pp collisions at $\sqrt{s}$ = 13 TeV and correspond to a total integrated luminosity of 139 fb^{-1} [32]. The data are required to satisfy criteria that ensure that the detector was in good operating condition [33]. Monte Carlo (MC) simulation samples are used to model all the major backgrounds and the signal processes.

For the HVT interpretations of the ATLAS data, the production of Z' and W' bosons via quark–antiquark annihilation was modelled at leading-order (LO) accuracy by MadGraph5 2.3.3 [34] interfaced with Pythia 8.186 [35], which used the A14 set of tuned parameters [36] and the NNPDF2.3lo parton distribution function (PDF) set [37]. Events were generated for a range of resonance masses from 300 GeV to 5 TeV using the benchmark HVT *Model A*. Separate generation of signal events for HVT *Model A* and *Model B* is not necessary as both give rise to mass peaks in the Zh and Wh system with a width that is dominated by the experimental resolution. Higgs boson decays into $b\bar{b}$ or $c\bar{c}$ are considered, assuming the branching fractions $B\left(h \to b\bar{b}/c\bar{c}\right) = 0.569/0.0287$ and a Higgs boson mass of $m_h = 125$ GeV. Even though this search does not target the decay $h \to c\bar{c}$ directly, it is sensitive to such events. The Z and W bosons were required to decay via $Z \to \nu\bar{\nu}$, $Z \to \ell^+\ell^-$, or $W \to \ell^\pm\nu$, with $\ell = e, \mu$, and τ. Contributions from $Z' \to WW \to \ell^\pm\nu qq$ or $W' \to WZ \to \ell^\pm\nu qq, \ell^+\ell^- qq$ decays are negligible to these searches.

For the 2HDM interpretations of the ATLAS data, events for the gluon–gluon fusion production of A bosons (ggA) were generated in the narrow-width approximation with MadGraph5 2.3.3 at LO accuracy and interfaced to Pythia 8.186, which used the A14 tune and the NNPDF2.3lo PDF set. Events for b-quark associated production of A bosons ($b\bar{b}A$) were simulated with MadGraph5_aMC@NLO 2.2.3 [34] using the four-flavour scheme at next-to-leading order (NLO) with massive b-quarks and the CT10nlo nf4 PDF set, and interfaced with Pythia 8.186, which used the A14 set of tuned parameters. Events were generated for a range of A boson masses from 220 GeV to 2 TeV, assuming a narrow width. In the 2HDM, the Higgs boson branching fractions vary strongly as a function of the relevant model parameters, and therefore the A boson signals were generated only for decays of the Higgs boson h into a $b\bar{b}$ pair. The Z boson was required to decay either via $Z \to \nu\bar{\nu}$ or via $Z \to \ell^+\ell^-$.

The production of W and Z bosons in association with jets was modelled by Sherpa 2.2.1 [38] with the NNPDF3.0nlo set of PDFs [39]. Diagrams with up to two additional parton emissions were simulated at NLO precision, and those with three or four additional parton emissions at LO accuracy, using the Comix [40] and OpenLoops [41–43] libraries. Matrix elements (ME) were merged with the Sherpa parton shower [44] (PS) using the MEPS@NLO prescription [45–48] and the set of tuned parameters developed by the Sherpa authors. The inclusive production cross section for these samples was normalised to match a next-to-next-to-leading-order (NNLO) prediction [49].

The production of top-quark pair ($t\bar{t}$) events was modelled using the Powheg Box v2 [50–53] generator. The matrix elements were calculated at NLO precision in QCD using the five-flavour scheme and the NNPDF3.0nlo PDF set, assuming a top-quark mass of 172.5 GeV. The PS, hadronisation, and underlying event were modelled with the Pythia 8.230 [54] generator using the A14 set of tuned parameters and the NNPDF2.3lo set of PDFs. The h_{damp} parameter[3] was set to 1.5 m_{top} [55]. The cross section was calculated at NNLO precision, including the resummation of next-to-next-to-leading logarithmic (NNLL) soft gluon terms with Top++ 2.0 [56–62].

[3] The h_{damp} parameter is a resummation damping factor and one of the parameters that control the matching of Powheg matrix elements to the PS, effectively regulating the high-p_{T} radiation against which the $t\bar{t}$ system recoils.

The $t\bar{t} + h$ samples were generated at NLO accuracy using the MadGraph5_aMC@NLO 2.3.2 generator with the NNPDF3.0nlo PDF set and interfaced to Pythia 8.186, which used the A14 set of tuned parameters and the NNPDF2.3lo PDF set.

The production of $t\bar{t} + V$ events (where $V = W, Z$) was modelled using the MadGraph5_aMC@NLO 2.3.3 generator at NLO with the NNPDF3.0nlo PDF set. The events were interfaced to Pythia 8.230, which used the A14 set of tuned parameters and the NNPDF2.3lo PDF set.

The associated production of top quarks with W bosons (Wt) and the s- and t-channel production of single top quarks were modelled by the Powheg Box v2 generator at NLO in QCD using the five-flavour scheme and the NNPDF3.0nlo set of PDFs. The diagram removal (DR) scheme [63] was used to remove interference and overlap with $t\bar{t}$ production. The events were interfaced to Pythia 8.230, which used the A14 set of tuned parameters and the NNPDF2.3lo set of PDFs.

Diboson events (WW, WZ, ZZ) with semileptonic decays were simulated using Sherpa 2.2.1 with the NNPDF3.0nnlo PDF set, including off-shell effects and Higgs boson contributions where appropriate. Diagrams with up to one additional emission were calculated at NLO accuracy in QCD, while diagrams with two or three parton emissions were described at LO accuracy [64]. They were merged and matched using the MEPS@NLO prescription. Loop-induced diboson processes that are initiated via the gg production mode were simulated at LO in QCD for diagrams with up to one additional parton emission in the matrix element using OpenLoops in Sherpa 2.2.2, which used the NNPDF3.0nnlo PDF set. Diboson events with fully leptonic decays were modelled using Sherpa 2.2.2 and the NNPDF3.0nnlo PDF set.

Finally, the production of a SM Higgs boson in association with a vector boson was simulated using Powheg Box v2, interfaced with Pythia 8.212 for PS and non-perturbative effects. The Powheg prediction is accurate to next-to-leading order for production of Vh plus one jet. The loop-induced $gg \to Zh$ process was generated separately at LO. The PDF4LHC15 PDF set [65] and the AZNLO set of tuned parameters [66] of Pythia 8.212 were used. The $gg \to Zh$ production cross section was calculated at NLO precision, including the resummation of next-to-leading logarithmic (NLL) soft gluon terms [67]. For the generation of Vh events, the Higgs boson mass was set to 125 GeV.

A summary of MC generators and programs used to model the underlying event and parton shower (UEPS) for the simulation of background processes is provided in Table 1.

All simulated event samples include the effect of multiple pp interactions in the same and neighbouring bunch crossings (pile-up) by overlaying simulated minimum-bias events on each generated signal or background event. The minimum-bias events were simulated with the single-, double- and non-diffractive pp processes of Pythia 8.186 using the A3 set of tuned parameters [68] and the NNPDF2.3lo PDF. For all MadGraph and Powheg Box samples, the EvtGen 1.6.0 program [69] was used for the bottom and charm hadron decays. The generated samples were processed using the Geant4-based ATLAS detector simulation [70, 71] and the simulated events were reconstructed using the same algorithms as were used for the data events.

Simulated events were corrected to compensate for differences between data and simulations regarding the energy (or momentum) scale and resolution of leptons and jets, the efficiencies for the reconstruction, identification, isolation and triggering of leptons, and the tagging efficiency for heavy-flavour jets.

Table 1: Summary of the Monte Carlo generators used to produce the various background processes. The perturbative accuracy (in QCD and, if relevant, in EW corrections) of the total production cross section σ_{prod} is stated for each process. The order at which the corresponding matrix elements are calculated in the Monte Carlo simulation is not necessarily the same as for the cross section. Details on the final state are also provided, where $\ell = e, \mu$, and τ.

Process	Generator	Perturbative accuracy of σ_{prod}
$q\bar{q} \to Z' \to Zh \to \ell\ell/\nu\nu + bb/cc$	MadGraph5 2.3.3 + Pythia 8.186	LO
$q\bar{q} \to W' \to Wh \to \ell\nu + bb/cc$	MadGraph5 2.3.3 + Pythia 8.186	LO
$gg \to A \to Zh \to \ell\ell/\nu\nu + bb$	MadGraph5 2.3.3 + Pythia 8.186	LO
$gg \to b\bar{b}A \to Zh \to \ell\ell/\nu\nu + bb$	MadGraph5_aMC@NLO 2.2.3 + Pythia 8.186	NLO
$W \to \ell\nu, Z \to \ell\ell, Z \to \nu\nu$	Sherpa 2.2.1	NNLO
$t\bar{t}$	Powheg Box v2 + Pythia 8.230	NNLO+NNLL
single top quarks (s- and t-channels)	Powheg Box v2 + Pythia 8.230	NLO
single top quarks (Wt-channel)	Powheg Box v2 + Pythia 8.230	approx. NNLO
$t\bar{t} + h$	MadGraph5_aMC@NLO 2.3.2 + Pythia 8.186	NLO (QCD) and NLO (EW)
$t\bar{t} + V$	MadGraph5_aMC@NLO 2.3.3 + Pythia 8.230	NLO
$qg/q\bar{q} \to VV \to \ell\ell/\ell\nu/\nu\nu + q\bar{q}$	Sherpa 2.2.1	NLO
$gg \to VV \to \ell\ell/\ell\nu/\nu\nu + q\bar{q}$	Sherpa 2.2.2	NLO
$qg/q\bar{q} \to \ell\ell\nu\nu$	Sherpa 2.2.2	NLO
$qq \to Wh \to \ell\nu + b\bar{b}$	Powheg Box v2 + Pythia 8.212	NNLO (QCD) and NLO (EW)
$qq \to Zh \to \ell\ell/\nu\nu + b\bar{b}$	Powheg Box v2 + Pythia 8.212	NNLO (QCD) and NLO (EW)
$gg \to Zh \to \ell\ell/\nu\nu + b\bar{b}$	Powheg Box v2 + Pythia 8.212	NLO+NLL

4 Event reconstruction

Collision vertices are reconstructed from at least two ID tracks, each with a transverse momentum $p_{\text{T}} > 500$ MeV [72]. Among all vertices, the one with the highest p_{T}^2 sum of all associated tracks is chosen to be the primary vertex (PV) of the event.

Electrons are reconstructed from ID tracks that are matched to energy clusters in the electromagnetic calorimeter and which originate from the PV. The latter condition is satisfied by a requirement on the transverse impact parameter significance, $|d_0|/\sigma(d_0) < 5.0$, and on the longitudinal impact parameter, $|z_0 \sin(\theta)| < 0.5$ mm. Electrons must satisfy requirements for the electromagnetic shower shape, track quality, and track–cluster matching, using a likelihood-based approach. A *Tight* operating point is used for the 1-lepton channel and a *Loose* operating point is used for the 2-lepton channel as well as the electron veto in the 0-lepton channel [73]. Electrons also have to be isolated from hadronic activity in the event: both the transverse energy sum and the scalar sum of transverse momenta of all ID tracks within a cone of variable size around the electron have to be smaller than 0.06 times the electron's transverse energy E_{T}. The maximum cone size is $\Delta R = 0.2$, shrinking for larger E_{T} [73]. Electron candidates are required to have a minimum p_{T} of 7 GeV and to lie within $|\eta| < 2.47$.

Muons [74] are identified by matching tracks found in the ID to either energy deposits in the calorimeter system consistent with a minimum-ionising particle (*calorimeter-tagged muons*) or full tracks (*combined muons*) or track segments (*segment-tagged muons*) reconstructed in the muon spectrometer. Muons reconstructed as stand-alone tracks in the muon spectrometer are also considered. Like electrons, they have to fulfil impact-parameter requirements: $|d_0|/\sigma(d_0) < 3.0$ and $|z_0 \sin(\theta)| < 0.5$ mm. Muons are required to pass the *Tight* identification operating point for the 1-lepton channel or the *Loose* identification

operation point for both the 2-lepton channel and the muon veto in the 0-lepton channel. Muon candidates with $p_{\mathrm{T}} > 300$ GeV must satisfy tighter identification requirements in the muon spectrometer in order to improve the p_{T} resolution [74]. Muons must also be isolated: in the ID system, the p_{T} sum within a variable-size cone around the combined track has to be smaller than 0.06 times the muon's transverse momentum. The maximum cone size is $\Delta R = 0.3$, shrinking for larger muon p_{T}. Muon candidates are required to have a minimum p_{T} of 7 GeV and to lie within $|\eta| < 2.5$.

Three jet types are reconstructed, using the anti-k_t [75] algorithm implemented in the FastJet package [76]. Small-R jets are reconstructed from noise-suppressed topological clusters in the calorimeter [77, 78] using a radius parameter of $R = 0.4$. They are required to have $p_{\mathrm{T}} > 20$ GeV for central jets ($|\eta| < 2.5$) and $p_{\mathrm{T}} > 30$ GeV for forward jets ($2.5 < |\eta| < 4.5$). To suppress central jets from pile-up interactions, they are required to pass the jet vertex tagger [79] selection if they have $p_{\mathrm{T}} < 120$ GeV and $|\eta| < 2.5$. Large-R jets are used to reconstruct high-momentum Higgs boson candidates, for which the b-quarks are emitted with small angular separation. These jets are built using a radius parameter of $R = 1.0$ and a combination of ID tracks and calibrated clusters of energy deposits in calorimeter cells, referred to as Track-CaloClusters [80]. Trimming [81] is applied to remove the energy of clusters that originate from initial-state radiation, pile-up interactions or the underlying event. This is done by reclustering the constituents of the initial jet, using the k_t algorithm [82, 83], into smaller $R_{\mathrm{sub}} = 0.2$ subjets and then removing any subjet that has a p_{T} less than 5% of the p_{T} of the parent jet [84]. The large-R jets are required to have $p_{\mathrm{T}} > 250$ GeV and $|\eta| < 2.0$. The momenta of both the large-R and small-R jets are corrected for energy losses in passive material and for the non-compensating response of the calorimeter. Small-R jets are also corrected for the average additional energy due to pile-up interactions [85, 86]. The third type of jets are clustered from ID tracks using a variable radius (VR) that shrinks with increasing p_{T} of the studied proto-jet [87]. VR track-jets are used in this analysis to identify b-jets from decays of boosted Higgs bosons. They must contain at least two ID tracks compatible with the primary vertex and must have $p_{\mathrm{T}} > 10$ GeV as well as $|\eta| < 2.5$. In this analysis, only large-R jets with at least one ghost-associated [88] VR track-jet are retained.

Small-R jets and VR track-jets containing b-hadrons are identified using the MV2c10 b-tagging algorithm [89–92], with an operating point that corresponds to a selection efficiency for b-jets of 70%, as measured in simulated $t\bar{t}$ events. Applying the b-tagging algorithm reduces the number of light-flavour and gluon jets, jets containing hadronically decaying τ-leptons, and c-quark jets, by a factor of 300 (304), 36 (55) and 9 (9), respectively, for small-R jets (VR track-jets) [89].

Hadronically decaying τ-lepton candidates [93, 94] are used in the $\nu\bar{\nu}b\bar{b}$ channel to reject backgrounds with real hadronically decaying τ-leptons. They are reconstructed using calorimeter-based small-R jets. They are required to have either one or three associated tracks, $p_{\mathrm{T}} > 20$ GeV and $|\eta| < 1.37$ or $1.52 < |\eta| < 2.5$. They are identified using a multivariate tagging algorithm, which is 55% (40%) efficient for one-track (three-track) τ-lepton candidates [94].

The missing transverse momentum, with magnitude $E_{\mathrm{T}}^{\mathrm{miss}}$, is calculated as the negative vector sum of the transverse momenta of calibrated leptons and jets, plus a track-based soft term, i.e. all tracks compatible with the primary vertex and not associated with any lepton or jet used in the $E_{\mathrm{T}}^{\mathrm{miss}}$ calculation [95, 96]. In addition, a track-based missing transverse momentum estimator $\vec{p}_{\mathrm{T}}^{\,\mathrm{miss}}$ is built as the negative vector sum of the transverse momenta of all tracks from the primary vertex. In order to reduce backgrounds from mismeasurements of jet and lepton energies, an object-based $E_{\mathrm{T}}^{\mathrm{miss}}$ significance $\mathcal{S}$ [97] is exploited. This observable takes the resolutions of objects entering the $E_{\mathrm{T}}^{\mathrm{miss}}$ calculation into account and quantifies how likely it is that there is significant $E_{\mathrm{T}}^{\mathrm{miss}}$ from undetectable particles (such as neutrinos).

Electrons, muons, hadronically decaying τ-leptons and jets are reconstructed and identified independently. This can lead to ambiguous identifications when these objects are spatially close to each other. An overlap removal procedure is therefore applied to uniquely identify these objects. Small-R jets are discarded if they are within a cone of size $\Delta R = 0.2$ around an electron or τ-lepton or if they have fewer than three associated tracks and are within a cone of $\Delta R = 0.2$ around a muon candidate. A τ-lepton is removed if it is within a cone of $\Delta R = 0.2$ around an electron or a muon. Finally, electrons and muons are discarded if they are within $\Delta R = \min(0.4, 0.04 + 10\,\text{GeV}/p_{\text{T}}^{\ell})$ of the axis of any surviving jet, where p_{T}^{ℓ} is the transverse momentum of the electron or muon.

Two dedicated correction procedures are applied to improve the mass resolution of the reconstructed Higgs boson candidates. If any muons are found within a cone of p_{T}-dependent size around the jet axis, the four-momentum of the closest muon in ΔR with p_{T} larger than 5 GeV is added to the jet four-momentum after subtracting the energy contribution deposited in the calorimeter by the muon [22, 98] (refered to as the muon-in-jet correction). For this correction, muons are not required to pass any isolation requirements. Additional flavour-specific energy corrections are applied, after the standard jet-energy-scale calibration [85], to both b-tagged small-R and large-R jets to account for biases in the response to jets with leptonic or hadronic decays of heavy-flavour hadrons (refered to as the p_{T}-reconstruction correction). The p_{T}-reconstruction corrections are determined from simulated SM $Vh(h \to b\bar{b})$ events by calculating the ratio of the p_{T} of the generator-level b-jets from the Higgs boson decay to the p_{T} of the reconstructed b-tagged jets after the muon-in-jet correction is applied.

5 Analysis strategy and event selection

The search for the Z' and A bosons in the $Zh \to \nu\bar{\nu}b\bar{b}$ and $Zh \to \ell^+\ell^- b\bar{b}$ decay modes uses event selections wherein the number of reconstructed charged leptons is exactly zero or two (0-lepton and 2-lepton channels). In the 0-lepton channel, large $E_{\text{T}}^{\text{miss}}$ signals the presence of two neutrinos. For the W' search in the $Wh \to \ell^{\pm}\nu b\bar{b}$ channel, events with exactly zero or one charged lepton are used (0-lepton or 1-lepton channels).

For the 0-lepton channel and the 1-muon channel, $E_{\text{T}}^{\text{miss}}$ triggers [99] with thresholds of 70–110 GeV are used for the various data-taking periods, corresponding to the increasing instantaneous luminosity. The $E_{\text{T}}^{\text{miss}}$ triggers are more efficient than single-muon triggers for the relatively large momentum of the W boson required in the analysis[4] ($p_{\text{T},W} > 150$ GeV) [100]. The trigger efficiency is above 80% for events with $E_{\text{T}}^{\text{miss}} > 150$ GeV and essentially 100% above 200 GeV.

In the 2-lepton channel and the 1-electron channel, events were recorded using a combination of single-lepton triggers [101, 102] with isolation requirements. The lowest p_{T} thresholds range from 24 GeV to 26 GeV in the electron channel and from 20 GeV to 26 GeV in the muon channel. Additional triggers without an isolation requirement are used to recover efficiency for leptons with $p_{\text{T}} > 60$ (50) GeV in the electron (muon) channel. The trigger-level electron (muon) is required to match a reconstructed electron (muon) with $p_{\text{T}} > 27$ GeV. The trigger efficiencies for the combined single-electron and combined single-muon triggers are larger than 95%.

The Higgs boson candidate is reconstructed from the four-vectors of its decay products, the b-quarks. When the Higgs boson has relatively low p_{T}, the b-quarks can be reconstructed as two small-R jets (*resolved*

[4] Since muons are not included in the online $E_{\text{T}}^{\text{miss}}$ calculation, $E_{\text{T}}^{\text{miss}}$ and $p_{\text{T},W}$ are equivalent at the trigger level.

category). As the momentum of the Higgs boson increases, the two b-quarks become more collimated and a selection using a single large-R jet becomes more efficient (*merged* category).

For the resolved signal region, two central small-R jets are required to have an invariant mass m_{jj} in the range 110–140 GeV for the 0-lepton and 1-lepton channels and in the range 100–145 GeV for the 2-lepton channel. The latter selection is looser in order to take advantage of the lower background contribution in this channel. When two b-tagged jets are present in the event, the dijet system representing the Higgs boson candidate is defined by the two b-tagged small-R jets. In events with more than two b-tagged jets, the dijet system is defined by the two leading b-tagged jets. In the case where only one b-tagged jet is present, the dijet pair is defined by the b-tagged jet and the leading small-R jet in the remaining set. The leading jet in the pair must have $p_{\mathrm{T}} > 45$ GeV. For the merged signal region, a large-R jet is required with mass m_{J} in the range 75–145 GeV and at least one associated b-tagged VR track-jet. Events which satisfy the selection requirements of both the resolved and merged categories are assigned to the resolved category because of its better dijet mass resolution. In resolved event topologies, the four-momentum of the dijet system is scaled by 125 GeV / m_{jj}.

Higgs boson candidates with one or two b-tagged jets define the *1 b-tag* and *2 b-tags* categories, respectively. For the merged selection, only one or two leading VR track-jets associated with the large-R jet are considered in this counting. In the searches for Z', W' and A boson production via the ggA process, events with exactly one or exactly two b-tagged jets are considered, while signal production via the $b\bar{b}A$ process is addressed by introducing further categories for events with additional b-tagged jets. In the resolved region a category with at least three b-tagged jets (*3+ b-tags*) is used, while in the merged regions, events are assigned to additional categories based on the number of b-tagged VR track-jets outside of the large-R jet. The 0-lepton channel uses a category for events in which two b-tagged VR track-jets are associated with the large-R jet and at least one b-tagged VR track-jet is outside of the large-R jet (*2 b-tags & 1+ add*).[5] Furthermore, the 2-lepton channel uses a category in which at least one b-tagged VR track-jet is associated with the large-R jet and at least one b-tagged VR track-jet is outside of the large-R jet (*1+ b-tags & 1+ add*).

The calculation of the reconstructed mass m_{Vh} of the Vh resonance depends on the decay channel. In the 0-lepton channel, where it is not possible to fully reconstruct the Vh system, the transverse mass is used as the final discriminant, defined as: $m_{\mathrm{T},Vh} = \sqrt{\left(E_{\mathrm{T},h} + E_{\mathrm{T}}^{\mathrm{miss}}\right)^2 - \left(\vec{p}_{\mathrm{T},h} + \vec{E}_{\mathrm{T}}^{\mathrm{miss}}\right)^2}$, where $E_{\mathrm{T},h}$ is the transverse energy of the Higgs boson candidate, while $\vec{E}_{\mathrm{T}}^{\mathrm{miss}}$ and $\vec{p}_{\mathrm{T},h}$ are vectors of the missing transverse momentum and Higgs boson transverse momentum, respectively. In the 1-lepton and 2-lepton channels, m_{Vh} is defined as the invariant mass calculated from the sum of four-momenta of the vector boson and Higgs boson candidates. In the 1-lepton channel, the vector boson is reconstructed from the sum of the four-momenta of the charged lepton and the neutrino. The momentum of the neutrino in the z-direction, $p_{z,\nu}$, is obtained by imposing a W boson mass constraint on the lepton–neutrino system, which results in a quadratic equation. Here $p_{z,\nu}$ is taken as either the real component of the complex solutions or the real solution with the smaller absolute magnitude. The transverse mass of the W boson, $m_{\mathrm{T},W}$, is calculated from the transverse component of the lepton momentum and the $\vec{E}_{\mathrm{T}}^{\mathrm{miss}}$. In the 2-lepton channel, the vector boson is reconstructed from the sum of the four-momenta of the two charged leptons. In events with two muons, the mass resolution in the signal region is improved by scaling the four-momentum of the dimuon system by 91.2 GeV / $m_{\mu\mu}$ to account for poorer dimuon mass resolution at high p_{T}.

[5] The category for events with exactly one b-tagged VR track-jet associated with the large-R jet and at least one b-tagged VR track-jet outside of the large-R jet (i.e. *1 b-tag & 1+ add*) does not add sensitivity to the 0-lepton channel and is therefore not used for the A boson search.

An event-cleaning procedure is applied to all lepton channels. Events are removed if they contain overlaps between one of the VR track-jets used for b-tagging and at least one VR track-jet with a p_{T} above 5 GeV and with at least two associated tracks, in order to prevent the selection of jets with ambiguously matched tracks from heavy-flavour hadron decays. Additional selections are applied for each lepton channel, as outlined below, to reduce the main backgrounds and enhance the signal sensitivity.

The 0-lepton channel vetoes electrons and muons and, for the Z', ggA and $b\bar{b}A$ searches, also hadronically decaying τ-lepton candidates (τ_{had}). In order to recover $W' \to Wh \to \tau_{\mathrm{had}}\nu bb$ events via the 0-lepton channel, the veto on τ_{had} is relaxed for the W' search such that events with at most one τ_{had} are selected. The multijet background is reduced by requiring a missing transverse momentum of $E_{\mathrm{T}}^{\mathrm{miss}} > 150$ (200) GeV in the resolved (merged) category, an $E_{\mathrm{T}}^{\mathrm{miss}}$ significance $\mathcal{S}$ of 9.0–13.6, increasing linearly as a function of $m_{\mathrm{T},Vh}$, a track-based missing transverse momentum of $p_{\mathrm{T}}^{\mathrm{miss}} > 60$ GeV, an angular separation between $E_{\mathrm{T}}^{\mathrm{miss}}$ and $p_{\mathrm{T}}^{\mathrm{miss}}$ of $\Delta\phi(\vec{E}_{\mathrm{T}}^{\mathrm{miss}}, \vec{p}_{\mathrm{T}}^{\mathrm{miss}}) < \pi/2$, an angular separation between $E_{\mathrm{T}}^{\mathrm{miss}}$ and the Higgs boson candidate of $\Delta\phi(\vec{E}_{\mathrm{T}}^{\mathrm{miss}}, h) > 2\pi/3$, and the minimum angular separation between $E_{\mathrm{T}}^{\mathrm{miss}}$ and the jets that are used in the event to satisfy $\min\left[\Delta\phi(\vec{E}_{\mathrm{T}}^{\mathrm{miss}}, \text{small-}R\text{ jet})\right] > \pi/9$ ($\pi/6$) for events with up to three (more than three) jets. In the resolved channel, the angular separation between the two Higgs boson candidate jets is required to be $\Delta\phi_{jj} < 7\pi/9$, and the scalar sum of all jet p_{T} values must satisfy $S_{\mathrm{T}} > 120$ (150) GeV if the event contains two (more than two) central jets. Finally, the resolved channel requires at least two central small-R jets, and the merged channel at least one large-R jet.

For the 1-lepton channel, selected events are required to have exactly one electron or one muon with $p_{\mathrm{T}} > 27$ GeV. The multijet background is reduced by requiring $E_{\mathrm{T}}^{\mathrm{miss}} > 80\,(40)$ GeV for events with an electron (muon) in the resolved category, and in the merged category the requirement is increased to $E_{\mathrm{T}}^{\mathrm{miss}} > 100$ GeV for both electrons and muons. A m_{Wh}-dependent requirement is placed on $p_{\mathrm{T},W}$: it has to be larger than both 150 GeV and $\left[710 - (3.3 \cdot 10^5)/m_{Wh}\right]$ GeV for the resolved channel, and larger than both 150 GeV and $\left[394 \cdot \ln(m_{Wh}) - 2350\right]$ GeV for the merged channel, where m_{Wh} is expressed in GeV. The selection requirements on $p_{\mathrm{T},W}$ exploit the fact that the m_{Wh} and $p_{\mathrm{T},W}$ observables are more strongly correlated for the signal process than for the various backgrounds. Finally, the transverse mass of the W boson candidate is required to be less than 300 GeV in order to remove events in which the $E_{\mathrm{T}}^{\mathrm{miss}}$ or lepton momentum is not well reconstructed. In addition, the angular separation between the charged lepton and the Higgs boson candidate must fulfil $\Delta R(\ell, h) > 2.0$.

In the 2-lepton channel, same-flavour leptons (ee or $\mu\mu$) are selected with $p_{\mathrm{T}} > 27$ GeV for the leading lepton and $p_{\mathrm{T}} > 20$ (25) GeV for the subleading lepton in the resolved (merged) category. Three kinematic selections are optimised as a function of the resonance mass m_{Vh} to reduce the $t\bar{t}$ and Z + jets backgrounds. The selection requirement on the mass of the dilepton system, $\max[40\text{ GeV},\ 87\text{ GeV} - 0.030 \cdot m_{Vh}] < m_{\ell\ell} < 97\text{ GeV} + 0.013 \cdot m_{Vh}$, and the requirement $E_{\mathrm{T}}^{\mathrm{miss}}/\sqrt{H_{\mathrm{T}}} < 1.15 + (8 \times 10^{-3}) \cdot m_{Vh}\,/\,(1\text{ GeV})$ vary as a function of the m_{Vh}, and these requirements become looser for larger resonance masses to account for smaller backgrounds and a degradation of the dilepton invariant mass and energy resolution with increasing boost of the final-state particles. The H_{T} is calculated as the scalar sum of the p_{T} of the leptons and small-R jets in the event. For the third kinematic selection, the momentum of the dilepton system ($p_{\mathrm{T},\ell\ell}$) is required to be greater than $\left[20 + 9 \cdot \sqrt{m_{Vh}/(1\text{ GeV}) - 320}\right]$ GeV for m_{Vh} greater than 320 GeV. In the resolved dimuon category, an opposite-charge requirement is applied to further reduce diboson backgrounds and because the probability of mismeasuring the charge of individual muons is very low.

All signal-region selections are summarised in Table 2. The products of kinematic acceptance and

reconstruction efficiency for $Z' \to Zh(h \to b\bar{b}/c\bar{c})$, $b\bar{b}A \to Zh(h \to b\bar{b})$ and $W' \to Wh(h \to b\bar{b}/c\bar{c})$ are shown in Figure 2 as a function of the resonance mass. The m_{Vh} resolution is expected to be in the range 2%–5% (5%–9%) for the resolved (merged) $\ell^+\ell^- b\bar{b}$ channel and in the range 7%–12% (9%–12%) for the resolved (merged) $\ell^\pm \nu b\bar{b}$ channel, while the $m_{\mathrm{T},Vh}$ resolution is expected to range from 8% to about 28% (from 12% to 17%) for the resolved (merged) $\nu\bar{\nu}b\bar{b}$ channel. The resolution of the $m_{\mathrm{T},Vh}$ and m_{Vh} deteriorates in the resolved (merged) category with increasing (decreasing) resonance mass.

In addition to the signal regions, dedicated control regions are used to improve the modelling of major backgrounds. These control regions are constructed by inverting one of the selection requirements of the signal region: in the 2-lepton resolved category, $t\bar{t}$ control regions are created by selecting events with different-flavour oppositely charged leptons $e\mu$, and without the $E_{\mathrm{T}}^{\mathrm{miss}}/\sqrt{H_{\mathrm{T}}}$ requirement. The $t\bar{t}$ purity of this selection is greater than 90%. These events are used to constrain the $t\bar{t}$ normalisation in the final fit. Dedicated m_{jj} (m_{J}) sideband regions are defined in the resolved (merged) 0- and 1-lepton regions by requiring m_{jj} (m_{J}) to be between 50 GeV and 200 GeV but outside the respective signal-region windows defined above. They are used to improve the modelling of the W/Z + jets kinematics and to constrain the normalisation of the $t\bar{t}$ and W/Z + jets backgrounds. As the Z + jets backgrounds are by far the largest in the 2-lepton signal region, yielding up to 90% of the total background, and due to the significant shape difference between the m_{Vh} templates for the hypothetical signal processes and the Z + jets backgrounds, no additional control regions are required to constrain the Z + jets contributions. Thus, the 2-lepton m_{jj} and m_{J} sideband regions are not included into the likelihood fit. Instead, these sidebands are used to correct the kinematics of the Z + jets background (see Section 6). The channels and regions used for the different fits are detailed in Table 3.

Table 2: Topological and kinematic selections for each channel and category as described in the text. $^{(*)}$ Applies in the case of only two central jets. $^{(**)}$ Applied only for the W' search. $^{(\dagger)}$ A higher threshold (80 GeV) is used for the single-electron channel. $^{(\dagger\dagger)}$ Applied only for $m_{Vh} > 320$ GeV. $^{(\ddagger\ddagger)}$ Only the two leading VR track-jets matched by ghost-association to the large-R jet are considered when classifying events into b-tag categories. Events are further classified according to the number of b-tagged jets in the events.

Variable	Resolved	Merged
	Common selection	
Number of jets	≥2 small-R jets (0, 2-lep.) 2 or 3 small-R jets (1-lep.)	≥1 large-R jet ≥ 1 VR track-jets (matched to leading large-R jet)‡‡
Leading jet p_{T} [GeV]	> 45	> 250
m_h [GeV]	110–140 (0,1-lep.), 100–145 (2-lep.)	75–145
	0-lepton selection	
$E_{\mathrm{T}}^{\mathrm{miss}}$ [GeV]	> 150	> 200
S_{T} [GeV]	> 150 (120^{*})	–
$\Delta\phi_{jj}$	$< 7\pi/9$	–
$p_{\mathrm{T}}^{\mathrm{miss}}$ [GeV]	> 60	
$\Delta\phi(\vec{E}_{\mathrm{T}}^{\mathrm{miss}}, \vec{p}_{\mathrm{T}}^{\mathrm{miss}})$	$< \pi/2$	
$\Delta\phi(\vec{E}_{\mathrm{T}}^{\mathrm{miss}}, h)$	$> 2\pi/3$	
$\min\left[\Delta\phi(\vec{E}_{\mathrm{T}}^{\mathrm{miss}}, \text{small-}R\text{ jet})\right]$	$> \pi/9$ (2 or 3 jets), $> \pi/6$ (≥ 4 jets)	
$N_{\tau_{\mathrm{had}}}$	0 ($\leq 1^{**}$)	
$E_{\mathrm{T}}^{\mathrm{miss}}$ significance $\mathcal{S}$	$\begin{cases} > 9 & \text{if } m_{Vh} < 240\,\text{GeV}, \\ > 6.6 + 0.01 \cdot m_{Vh} & \text{if } 240\,\text{GeV} \leq m_{Vh} < 700\,\text{GeV}, \\ > 13.6 & \text{if } m_{Vh} > 700\,\text{GeV}, \end{cases}$	
	1-lepton selection	
Leading lepton p_{T} [GeV]	> 27	> 27
$E_{\mathrm{T}}^{\mathrm{miss}}$ [GeV]	> 40 ($80^{\dagger}$)	> 100
$p_{\mathrm{T},W}$ [GeV]	$> \max\left[150,\ 710 - (3.3 \cdot 10^5\ \text{GeV})/m_{Vh}\right]$	$> \max\left[150,\ 394 \cdot \log(m_{Vh}/(1\,\text{GeV})) - 2350\right]$
$m_{\mathrm{T},W}$ [GeV]	< 300	
$\Delta R(\ell, h)$	> 2.0	
	2-lepton selection	
Leading lepton p_{T} [GeV]	> 27	> 27
Subleading lepton p_{T} [GeV]	> 20	> 25
$E_{\mathrm{T}}^{\mathrm{miss}}/\sqrt{H_{\mathrm{T}}}$ [$\sqrt{\text{GeV}}$]	$< 1.15 + 8 \times 10^{-3} \cdot m_{Vh}/(1\,\text{GeV})$	
$p_{\mathrm{T},\ell\ell}$ [GeV]	$> 20 + 9 \cdot \sqrt{m_{Vh}/(1\,\text{GeV}) - 320}^{\dagger\dagger}$	
$m_{\ell\ell}$ [GeV]	$\in \left[\max\left[40\ ,\ 87 - 0.030 \cdot m_{Vh}/(1\,\text{GeV})\right], 97 + 0.013 \cdot m_{Vh}/(1\,\text{GeV})\right]$	

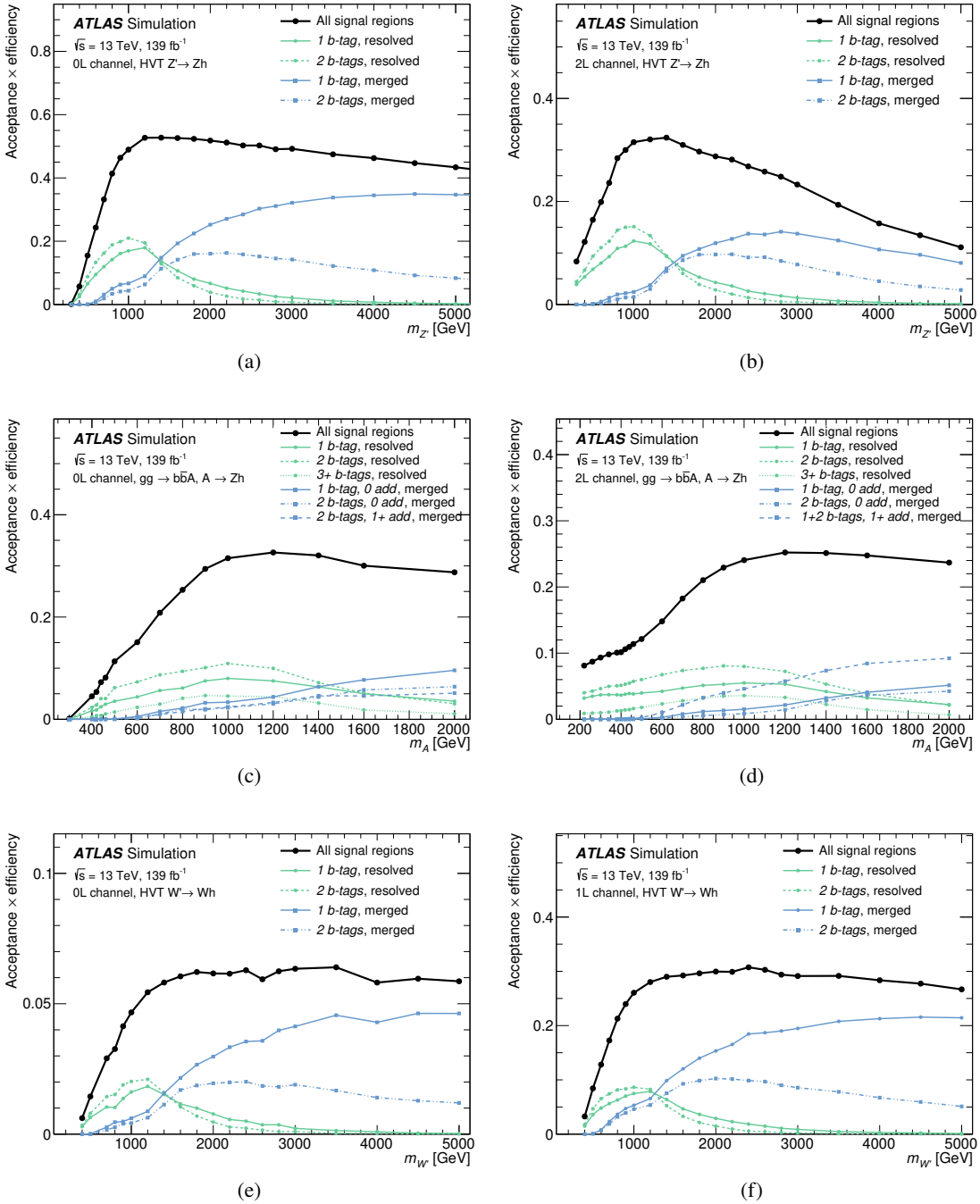

Figure 2: Product of acceptance and efficiency for (a) $Z' \to Zh \to \nu\bar{\nu}b\bar{b}/c\bar{c}$, (b) $Z' \to Zh \to \ell^+\ell^- b\bar{b}/c\bar{c}$, (c) $b\bar{b}A\,(\to Zh \to \nu\bar{\nu}b\bar{b})$, (d) $b\bar{b}A\,(\to Zh \to \ell^+\ell^- b\bar{b})$ and (e, f) $W' \to Wh \to \ell^{\pm}\nu b\bar{b}/c\bar{c}$ as a function of the resonance mass for the 0-lepton signal regions (a, c, e), the 2-lepton signal regions (b, d), and the 1-lepton signal regions (f).

Table 3: A list of the signal and control regions included in the statistical analysis of (a) the ggA, Z' and W' signal model hypotheses and (b) the $b\bar{b}A$ signal hypothesis. The searches for the pseudoscalar boson and the Z' boson are based on the 0- and 2-lepton channels, while the search for the W' boson is based on the 0- and 1-lepton channels. The notation 1+2 b-tag indicates that the 1 and 2 b-tag regions are combined.

(a) Signal and control regions for the ggA, $Z'$and W'searches

Channel	Region	Signal regions	Control regions	Signal hypotheses
		Resolved		
0-lepton	b-tags Mass window	*1, 2 b-tags* $110 < m_{jj}$ (GeV) < 140	*1, 2 b-tags* $50 < m_{jj}$ (GeV) < 110 || $140 < m_{jj}$ (GeV) < 200	ggA, Z', W'
1-lepton	b-tags Mass window	*1, 2 b-tags* $110 < m_{jj}$ (GeV) < 140	*1, 2 b-tags* $50 < m_{jj}$ (GeV) < 110 || $140 < m_{jj}$ (GeV) < 200	W'
2-lepton	b-tags Mass window Lepton flavour	*1, 2 b-tags* $100 < m_{jj}$ (GeV) < 145 ee, $\mu\mu$	*1 + 2 b-tags* $100 < m_{jj}$ (GeV) < 145 $e\mu$	ggA, Z'
		Merged		
0-lepton	b-tags Mass window	*1, 2 b-tags* $75 < m_{\mathrm{J}}$ (GeV) < 145	*1, 2 b-tags* $50 < m_{\mathrm{J}}$ (GeV) < 75 || $145 < m_{\mathrm{J}}$ (GeV) < 200	ggA, Z', W'
1-lepton	b-tags Mass window	*1, 2 b-tags* $75 < m_{\mathrm{J}}$ (GeV) < 145	*1, 2 b-tags* $50 < m_{\mathrm{J}}$ (GeV) < 75 || $145 < m_{\mathrm{J}}$ (GeV) < 200	W'
2-lepton	b-tags Mass window Lepton flavour	*1, 2 b-tags* $75 < m_{\mathrm{J}}$ (GeV) < 145 ee, $\mu\mu$	–	ggA, Z'

(b) Signal and control regions for the $b\bar{b}A$ search

Channel	Region	Signal regions	Control regions	Signal hypothesis
		Resolved		
0-lepton	b-tags Mass window	*1, 2, 3+ b-tags* $110 < m_{jj}$ (GeV) < 140	–	$b\bar{b}A$
2-lepton	b-tags Mass window Lepton flavour	*1, 2, 3+ b-tags* $100 < m_{jj}$ (GeV) < 145 ee, $\mu\mu$	*1+2, 3+ b-tags* $100 < m_{jj}$ (GeV) < 145 $e\mu$	$b\bar{b}A$
		Merged		
0-lepton	b-tags Mass window	*1, 2 b-tag, 2 b-tags & 1+ add* $75 < m_{\mathrm{J}}$ (GeV) < 145	–	$b\bar{b}A$
2-lepton	b-tags Mass window Lepton flavour	*1, 2 b-tag, 1+ b-tags & 1+ add* $75 < m_{\mathrm{J}}$ (GeV) < 145 ee, $\mu\mu$	–	$b\bar{b}A$

6 Background estimation

The background composition in the signal region depends on the charged-lepton and b-jet multiplicities. In the 0-lepton channel, the dominant background sources are Z + jets and $t\bar{t}$ events, with a significant contribution from W+ jets. In the 2-lepton channel, Z + jets production is the dominant background followed by $t\bar{t}$ production. The dominant background sources for the 1-lepton channel are W+ jets and $t\bar{t}$. Contributions from diboson, SM Vh, $t\bar{t}+h$ and $t\bar{t}+V$ production are small in all channels.

Background contributions from multijet events were studied and found to be negligible for the 0-lepton channels, the 2-lepton channels and the merged 1-lepton channel, while a small multijet background contribution (a few per mille of the total background) is found in the resolved 1 b-tag category for the 1-lepton channel. This contribution is estimated using a data-driven method: a template is produced in a dedicated control region enriched with multijet events, constructed by inverting the lepton isolation requirements decribed in Section 4. The shape of the m_{Vh} template is obtained by subtracting the other backgrounds from data, assuming that the other background processes are well modelled in Monte Carlo simulation. The normalisation of the template is derived from a two-component fit (multijet and 'rest') to data in the m_{jj} sideband control region. Further details of the template method can be found in Ref. [100].

The other background distributions are estimated from the samples of simulated events, with normalisations of the main backgrounds estimated from the data. The simulated W/Z + jets samples are reweighted as a function of the transverse momentum of the dijet system, $p_{\mathrm{T},jj}$, based on fits to the data/simulation distribution in the m_{jj} sideband regions, defined in Section 5. In the 2-lepton channel, different $p_{\mathrm{T},jj}$ reweighting are derived for the 1 b-tag and 2 b-tag regions. The $p_{\mathrm{T},jj}$ reweighting functions are derived after accounting for differences in the overall normalisation between data and the simulations.

The $t\bar{t}$, single-top-quark, $t\bar{t}+V$ and $t\bar{t}+h$ processes are combined into one single component, which is referred to as the top-quark backgrounds. In the search for a pseudoscalar produced via the $b\bar{b}A$ mode, the top-quark backgrounds are split into two components. The categorisation is based on the flavour of the additional jets[6] in the event, following the same strategy as described in Ref. [103]. Events containing at least one b- or c-quark jet not originating from a top quark, W, Z or Higgs boson decay are classified as top + hf (with hf denoting 'heavy flavour'), while all other events are classified as top + lf (with lf denoting 'light flavour').

Simulated samples of W/Z + jets events are split into different jet-flavour components to help improve the grouping of the background components in the final fit because their contributions vary between the 1 b-tag and 2 b-tag categories. In the resolved category, the samples are split according to the generated flavour of the two small-R jets forming the Higgs boson candidate. In the merged category, they are split according to the generated flavour of the one or two leading track-jets associated with the large-R jet. The generated jet flavour is determined by counting generated heavy-flavour hadrons with $p_{\mathrm{T}} > 5$ GeV that are matched by ghost-association to the reconstructed jet. If a b-hadron is found, the jet is labelled as a b-jet, otherwise if a c-hadron is found the jet is labelled as a c-jet. If neither a b-hadron nor a c-hadron is associated with the reconstructed jet, it is labelled as a light-flavour jet. Based on this association scheme, the W/Z + jets simulated event samples are split into three components: W/Z + hf ($W/Z+b\bar{b}$, $W/Z+b\bar{c}$ and $W/Z+c\bar{c}$), W/Z + hl ($W/Z+b$l and $W/Z+c$l) and W/Z + lf; in this notation 'l' refers to a light-flavour jet. In the statistical analysis described in Section 8, the global normalisations of the Z + hf, Z + hl, W + hf and

[6] Generator-level particle jets are reconstructed from stable particles (i.e. particles with a mean lifetime of $\tau > 3 \cdot 10^{-11}$ seconds) using the anti-k_t algorithm with a radius parameter of $R = 0.4$. These jets are required to have $p_{\mathrm{T}} > 15$ GeV and $|\eta| < 4.5$.

W + hl components are determined via a fit to data, while the normalisation of the W/Z + lf component is taken from simulation. In the A boson interpretation, the Z + hf background normalisation in the 3+ b-tag region is determined from this region independently to account for decreased perturbative accuracy of the background predictions for events with additional heavy-flavour jets in the final state.

In the statistical analysis described in Section 8 the global normalisations of the dominant background contributions, i.e. the top-quark, W/Z + hf , and W/Z + hl backgrounds, are determined separately for the 0-, 1- and 2-lepton channels via a fit to data. In the 0- and 1-lepton channels, the m_{jj} (m_{J}) sideband regions are used to constrain the W/Z + jets and top-quark backgrounds in the resolved (merged) event categories. In the 2-lepton channel, an $e\mu$ control region is used for resolved event topologies to constrain the normalisation of the combined top-quark backgrounds.

7 Systematic uncertainties

The distributions of m_{Vh} and $m_{\mathrm{T},Vh}$ are affected by both experimental and modelling uncertainties, which enter the final fits as nuisance parameters. Uncertainties in the modelling of physics objects are correlated over signal and background processes, channels, kinematic regions and distributions of observables.

The largest experimental systematic uncertainties are associated with the calibration and resolution of the small-R and large-R jet energy and of the large-R jet mass. Further dominant uncertainties are related to the determination of the b-tagging efficiency and misidentification rate. The uncertainties in the small-R jet energy scale have contributions from in situ calibration studies, from the dependency on the pile-up activity, and from the flavour composition of jets [85, 86]. An additional uncertainty in the energy calibration of b- and c-jets is also used. The uncertainty in the scale and resolution of the large-R jet energy and mass is estimated by comparing the ratio of calorimeter-based to track-based measurements in dijet data and simulation [84, 104]. Differences in the b-tagging efficiency measured in data and simulation result in correction factors for b-jets, c-jets and light-flavour jets. Uncertainties in these correction factors are decomposed into uncorrelated components [89, 91, 92]. An additional term is included to extrapolate the measured uncertainties to the high-p_{T} region of interest. This term is calculated from simulated events by considering variations of the quantities affecting the b-tagging performance, such as the impact parameter resolution, percentage of tracks from random combinations of measurements in the ID, description of the detector material, and track multiplicity per jet.

Uncertainties in the reconstruction, identification, isolation and trigger efficiencies of muons [105], electrons [106] and τ-leptons [107] and in their energy scale and resolution have only a small impact on the result. Uncertainties in the $E_{\mathrm{T}}^{\mathrm{miss}}$ trigger efficiency are taken into account by following the approach described in Ref. [98].

The uncertainties in the energy scale and resolution of the small-R jets and leptons are propagated to the calculation of $E_{\mathrm{T}}^{\mathrm{miss}}$, which also has additional uncertainties from the modelling of the underlying event and the momentum scale, momentum resolution and reconstruction efficiency of the tracks used to compute the soft-term [95, 96]. Finally, a global luminosity uncertainty of 1.7% is applied to the normalisation of all simulated events [108, 109].

Theoretical uncertainties are derived for all simulated signal and background processes and lead to variations in the normalisation and shape of the templates used for the statistical analysis. These uncertainties are assessed by comparing nominal and alternative event generators and UEPS models. In general, the perturbative precision and the PDF sets used in these alternative configurations match those of the nominal

generators (unless explicitly stated). Uncertainties due to the PDF set parameterisation are evaluated using replica sets, and uncertainties due to missing higher orders are evaluated by varying appropriate scale parameters, as described below. Uncertainties due to the modelling of PDFs are evaluated for the signal processes and all relevant backgrounds by comparing the predictions of their nominal PDF set with those of alternative PDF sets and then comparing the maximum difference with the difference from the root-mean-square spread of the nominal replica sets. The larger of the two is taken as the uncertainty.

For the signal processes, uncertainties in the acceptance were derived by replacing the nominal PDF set by the MSTW2008LO [110] and CT10 [111] PDF sets, by using the eigenvariations of the PYTHIA 8.186 A14 set of tuned parameter values [36], and by replacing PYTHIA 8.186 by HERWIG 7.0.4 [112]. Renormalisation and factorisation scale variations are also considered for the signal processes. The effects of these variations are sizeable for both of the two A boson production modes and negligible for the Z' and W' signals. For all the A, Z' and W' signals, the total acceptance uncertainties are between 2% and 7%.

The modelling uncertainties in $t\bar{t}$ events are derived as follows. To assess potential uncertainties in the matching of the matrix element to the parton shower, the nominal sample is compared with a sample where POWHEG BOX is replaced by MADGRAPH5_AMC@NLO. The parton shower modelling uncertainty is assessed by replacing PYTHIA 8.230 by HERWIG 7.04 together with the H7UE set of tuned parameters [112]. The uncertainty in the modelling of initial-state radiation (ISR) is addressed by changing the renormalisation and factorisation scales by a factor of two in combination with the eigenvariations of the A14 set of tuned parameters. The uncertainty in the modelling of final-state radiation (FSR) is addressed by varying the FSR scale [36].

To account for the ambiguities in the interference between top-quark pair and Wt production, an alternative sample generated with POWHEG BOX and PYTHIA 8.230, based on the diagram subtraction (DS) scheme [63], is used. The difference between the DS and DR schemes for Wt production is considered as an additional systematic uncertainty.

The relative contributions of the single-top-quark, $t\bar{t}+V$ and $t\bar{t}+h$ processes to the combined top-quark background are varied by 19% for single top quarks and by 50% for $t\bar{t}+V$ and $t\bar{t}+h$ production.

For $W/Z+$jets backgrounds, the effects of scale uncertainties are estimated by varying the renormalisation and factorisation scales by a factor of two. In order to account for variations of both the matrix element and the parton shower, the nominal samples were compared with samples with LO-accurate matrix elements that contain up to four final-state partons generated with MADGRAPH5_AMC@NLO 2.2.2 using the NNPDF3.0NLO PDF set and interfaced to PYTHIA 8.186 [113] using the CKKW-L merging procedure [114, 115]. The A14 set of tuned parameters of PYTHIA is used with the NNPDF2.3LO PDF set. Decays of bottom and charm hadrons are performed by EVTGEN 1.2.0.

In the 1-lepton channel, additional *JetBinMigration* uncertainties in the $W+$jets backgrounds, based on Ref. [116], are derived to account for the modelling of the veto of additional jets in the selection. These uncertainties are evaluated by individually varying the contributions from $W+$jets events with either less than two jets or more than three jets at the generator level. In both cases, the contributions to the signal and control regions are varied upwards/downwards by 50%. Only the shape uncertainties are retained because the normalisations of $W+$jets backgrounds are allowed to float in the final fit.

For both the $t\bar{t}$ and $W/Z+$jets backgrounds, uncertainties in the PDF were determined by the standard deviation of the 100 NNPDF3.0NLO replicas, by using NNPDF3.0NLO PDFs with varied α_s [39], and by comparisons with the nominal MMHT2014NNLO and the CT14NNLO PDF sets [65].

For the major backgrounds, the theory uncertainties listed above translate into pre-fit probability distributions (priors) for nuisance parameters affecting the global cross section and/or acceptance, the acceptance ratios between different fit regions,[7] and the shape of the distribution of the final mass discriminant. For the diboson and SM Vh backgrounds, only a normalisation uncertainty is assigned, as these processes give only a relatively small contribution to the studied phase-space regions. This normalisation uncertainty covers effects on both the cross section and acceptance [117]. The largest pre-fit impact on the m_{Vh} distribution's slope for W/Z + jets comes from ME+PS variations (10%–20% over the mass range studied), from scale uncertainties (5%–10%) and from the comparison with alternative PDF replicas (5%). The largest pre-fit impacts on the m_{Vh} distribution's slope in $t\bar{t}$ simulation come from the parton shower modelling and the matching of the matrix element to the parton shower (5%–20%), the ISR and FSR (2%–10%) and the PDF uncertainties (up to 5%).

The multijet background gives only minor contributions (of a few per mille of the total background) to the 1 b-tag signal and control regions of the 1-lepton channel. Various conservative uncertainties are assigned to the data-driven multijet background estimate (see Section 6): an uncertainty in the normalisation is set to 50% and an uncertainty in the shape is derived from the observed differences when varying the $E_{\mathrm{T}}^{\mathrm{miss}}$ selection requirement by ±25%. This variation yields a shape uncertainty of up to 40% for the m_{Vh} template. However, due to the small size of the multijet background, its uncertainties do not have a significant impact on the final results.

Additional uncertainties in the $p_{\mathrm{T},jj}$ reweighting of the W/Z + jets backgrounds in the 0-lepton and 2-lepton channels (see Section 6) are estimated from the full difference between the original and reweighted distributions. Residual mismodellings (i.e. non-closures in comparisons between data and simulation) of the $p_{\mathrm{T}}^{\mathrm{miss}}$ distribution in the 0-lepton channel, the $p_{\mathrm{T},W}$ distribution in the 1-lepton channel, and the transverse momentum of the leading large-R jet in all three channels, were observed in the respective m_{jj} and m_J sideband regions. The magnitude of these mismodellings depends on m_{Vh} and ranges from 1% to 10%. These are not corrected, but the data-to-simulation ratios are used to define systematic uncertainties in the relevant shapes and those are applied to all backgrounds as uncorrelated nuisance parameters.

The relative MC generator modelling systematic uncertainties (at the pre-fit stage), connected to the normalisation, cross-region extrapolation, and shape of the signal and background processes are detailed in Tables 4 and 5.

[7] Extrapolation effects between the signal and control regions, the resolved and merged categories, and the different lepton channels are taken into account.

Table 4: Relative MC generator modelling systematic uncertainties (at the pre-fit stage), connected to the normalisation, cross-region extrapolation, and shape of the W/Z + jets background processes included in the fits described in the text. An 'S' indicates that a shape variation is included for the sources listed, '$A \leftrightarrow B$' indicates an extrapolation uncertainty between the regions A and B, and 'norm.' is the sum of cross-section and acceptance variations. A value of 'float' indicates that the parameter is not constrained in the fit. The uncertainty in the normalisation ratios of two regions, determines to what degree the normalisations of two regions can diverge in the combined fit. A range of values means the value depends on the lepton channel. Parentheses indicate when the uncertainty applies only to a given fit or a given region.

Process	Quantity/source	Value
Z + hf	0/2 lep. norm.	float
	1-lep. norm.	50%
	0/2-lep. resolved ↔ merged	10%–19%
	1-lep. resolved ↔ merged	9%–18%
	0-lep. SR ↔ CR	5%–12%
	1-lep. SR ↔ CR	6%–20%
	0-lep. ↔ 1-lep.	7%–27%
	0-lep. ↔ 2-lep.	4%–16%
	generator, PDF, scale	S
	$p_{\mathrm{T},jj}$ reweighting	S
	$p_{\mathrm{T}}^{\mathrm{miss}}$ non-closure (0-lep.)	S
	$p_{\mathrm{T},W}$ non-closure (1-lep.)	S
	Large-R jet p_{T} non-closure	S
Z + hl	0/2 lep. norm.	float
	1-lep. norm.	50%
	0/2 lep. resolved ↔ merged	15%–28%
	1-lep. resolved ↔ merged	12%–13%
	0-lep. SR ↔ CR	3%–20%
	1-lep. SR ↔ CR	5%–7%
	0-lep. ↔ 1-lep.	7%–27%
	0-lep. ↔ 2-lep.	6%–17%
	generator, PDF, scale	S
	$p_{\mathrm{T},jj}$ reweighting	S
	$p_{\mathrm{T}}^{\mathrm{miss}}$ non-closure (0-lep.)	S
	$p_{\mathrm{T},W}$ non-closure (1-lep.)	S
	Large-R jet p_{T} non-closure	S
Z + lf	norm.	19%
	0/2 lep. resolved ↔ merged	8%–50%
	1-lep. resolved ↔ merged	10%–29%
	0-lep. SR ↔ CR	5%–20%
	1-lep. SR ↔ CR	29%–99%
	0-lep. ↔ 1-lep.	8%–39%
	0-lep. ↔ 2-lep.	4%–17%
	generator, PDF, scale	S
	$p_{\mathrm{T},jj}$ reweighting	S
	$p_{\mathrm{T}}^{\mathrm{miss}}$ non-closure (0-lep.)	S
	$p_{\mathrm{T},W}$ non-closure (1-lep.)	S
	Large-R jet p_{T} non-closure	S

Process	Quantity/source	Value
W + hf	0/2 lep. norm.	30%
	1-lep. norm.	float
	0/2 lep. resolved ↔ merged	13%–28%
	1-lep. resolved ↔ merged	15%–22%
	0-lep. SR ↔ CR	5%–28%
	1-lep. SR ↔ CR	3%
	0-lep. ↔ 1-lep.	4%
	generator, PDF, scale	S
	$p_{\mathrm{T},jj}$ reweighting (0-lep.)	S
	$p_{\mathrm{T}}^{\mathrm{miss}}$ non-closure (0-lep.)	S
	$p_{\mathrm{T},W}$ non-closure (1-lep.)	S
	Large-R jet p_{T} non-closure	S
	JetBinMigration (1-lep.)	S
W + hl	0/2 lep. norm.	30%
	1-lep. norm.	float
	0/2 lep. resolved ↔ merged	2%–43%
	1-lep. resolved ↔ merged	12%–13%
	0-lep. SR ↔ CR	2%–20%
	1-lep. SR ↔ CR	1%–2%
	0-lep. ↔ 1-lep.	4%
	generator, PDF, scale	S
	$p_{\mathrm{T},jj}$ reweighting (0-lep.)	S
	$p_{\mathrm{T}}^{\mathrm{miss}}$ non-closure (0-lep.)	S
	$p_{\mathrm{T},W}$ non-closure (1-lep.)	S
	Large-R jet p_{T} non-closure	S
	JetBinMigration (1-lep.)	S
W + lf	0/2 lep. norm.	20%
	1-lep. norm.	float
	0/2 lep. resolved ↔ merged	14%–18%
	1-lep. resolved ↔ merged	20%–21%
	0-lep. SR ↔ CR	4%–20%
	1-lep. SR ↔ CR	2%–4%
	generator, PDF, scale	S
	$p_{\mathrm{T},jj}$ reweighting (0-lep.)	S
	$p_{\mathrm{T}}^{\mathrm{miss}}$ non-closure (0-lep.)	S
	$p_{\mathrm{T},W}$ non-closure (1-lep.)	S
	Large-R jet p_{T} non-closure	S
	JetBinMigration (1-lep.)	S

Table 5: Relative MC generator modelling systematic uncertainties (at the pre-fit stage), connected to the normalisation, cross-region extrapolation, and shape of signal and the top, SM Vh and diboson background processes included in the fits described in the text. An 'S' indicates that a shape variation is included for the sources listed, '$A \leftrightarrow B$' indicates an extrapolation uncertainty between the regions A and B, and 'norm.' is the sum of cross section and acceptance variations. A value of 'float' indicates that the parameter is not constrained in the fit. The uncertainty in the normalisation ratios of two regions, determines to what degree the normalisations of two regions can diverge in the combined fit. A range of values means the value depends on the lepton channel. Parentheses indicate when the uncertainty applies only to a given fit or a given region.

Process	Quantity/source	Value
Signal	PS, ISR/FSR, PDF	2%–7%, S
SM Vh	0/1/2-lep norm.	32%
	$p_{\mathrm{T}}^{\mathrm{miss}}$ non-closure (0-lep.)	S
	$p_{\mathrm{T},W}$ non-closure (1-lep.)	S
	Large-R jet p_{T} non-closure	S
Diboson	0/1-lep norm.	50%
	2-lep norm.	20%
	$p_{\mathrm{T}}^{\mathrm{miss}}$ non-closure (0-lep.)	S
	$p_{\mathrm{T},W}$ non-closure (1-lep.)	S
	Large-R jet p_{T} non-closure	S

Process	Quantity/source	Value
Top quark	0/1/2-lep. norm. ($b\bar{b}A$: separate $t\bar{t}$ +hf norm.)	float
	single-top-quark contribution	19%
	$t\bar{t}+V$ contribution	50%
	$t\bar{t}+h$ contribution	50%
	0-lep. resolved $\leftrightarrow$ merged	9%–20%
	1-lep. resolved $\leftrightarrow$ merged	18%–20%
	2-lep. resolved $\leftrightarrow$ merged	18%
	0-lep. SR $\leftrightarrow$ CR	2%–12%
	1-lep. SR $\leftrightarrow$ CR	2%–3%
	2-lep. SR $\leftrightarrow$ CR	1.2%
	PS, ISR/FSR, ME, PDF	S
	DS vs DR scheme (Wt)	S
	$p_{\mathrm{T}}^{\mathrm{miss}}$ non-closure (0-lep.)	S
	$p_{\mathrm{T},W}$ non-closure (1-lep.)	S
	Large-R jet p_{T} non-closure	S

8 Results

In order to test for the presence of a massive resonance, the $m_{\mathrm{T},Vh}$ and m_{Vh} templates obtained from the signal and background simulated event samples are fitted to data using a binned maximum-likelihood approach based on the RooFit/RooStats framework [118–120]. Fits are simultaneously performed on the SRs and CRs defined in Table 3 in order to constrain the normalisation of backgrounds and the nuisance parameters (NPs) describing the systematic uncertainties detailed in Section 7. Each systematic variation enters the fit as an individual NP using a log-normal constraint so that the expected event yields remain positive for all values of the corresponding NPs (even for bins with low event counts). The correlations between systematic uncertainties are maintained across regions and processes. Fits are performed on the $m_{\mathrm{T},Vh}$ distribution in the 0-lepton channel and the m_{Vh} distribution in the 1-lepton and 2-lepton channels using a binning of the distributions chosen to optimise the search sensitivity while minimising statistical fluctuations. Asimov datasets [121] are used to evaluate the expected performance of each fit.

The results are expressed as upper limits at the 95% confidence level (CL) on the production cross section times branching fraction of Z', W', and A bosons for a wide range of resonance masses. The limits are evaluated using a modified frequentist method known as $\mathrm{CL_s}$ [122] and the profile-likelihood-ratio test statistic in an asymptotic approximation [121].

Different fit configurations (i.e. fit models) are used depending on the targeted signal hypothesis, production mode, or final state:

- Searches for heavy vector bosons produced via quark–antiquark annihilation:
  - The search for a Z' boson is based on a combined fit in the 0-lepton and 2-lepton channels. The signal cross section is a free parameter, as are the global normalisations of the top-quark, $Z+\text{hf}$ and $Z+\text{hl}$ backgrounds. Common normalisation factors are used for the $Z+\text{hf}$ and $Z+\text{hl}$ backgrounds, while the normalisation of the top-quark backgrounds is determined separately for the 0-lepton and 2-lepton event categories. The results of these searches are presented as one-dimensional upper limits at 95% CL on the production cross section times branching ratio, as well as constraints on the parameter space of the HVT model.
  - The search for a W' boson is based on a combined fit in the 0-lepton and 1-lepton channels. The signal cross section is a free parameter, as are the global normalisations of the top-quark, $Z+\text{hf}$, $Z+\text{hl}$, $W+\text{hf}$ and $W+\text{hl}$ backgrounds. Results are presented as one-dimensional upper limits at 95% confidence level on the production cross section times branching ratio, as well as constraints on the parameter space of the HVT model.
- Searches for a pseudoscalar A boson based on combined fits in the 0-lepton and 2-lepton channels.
  - The search for the gluon–gluon fusion production mode follows the same strategy as the search for the Z' boson.
  - In the search for the b-associated production mode, the signal cross section is a free parameter, as are the global normalisations of the top + lf, top + hf, $Z+\text{hf}$ and $Z+\text{hl}$ backgrounds. An additional normalisation factor is used for the $Z+$jets background contribution in the event categories with three or more b-tagged jets.
  - A simultaneous fit of the ggA and $b\bar{b}A$ signal hypotheses is performed for a variety of different $\sigma_{b\bar{b}A}$ and σ_{ggA} combinations. A negative log-likelihood (NLL) value is calculated for each $(\sigma_{b\bar{b}A}, \sigma_{ggA})$ combination, and the best estimate is obtained at the point where the NLL curve reaches its minimum. Contours at 68% and 95% CL are determined relative to the minimum. The background model is the same as for the $b\bar{b}A$ search.
  - A combined fit of the ggA and $b\bar{b}A$ production modes with one free parameter is performed to determine the total cross section of the two components. The fit is performed for different admixtures of ggA and $b\bar{b}A$ contributions, $\sigma_{b\bar{b}A}/(\sigma_{b\bar{b}A}+\sigma_{ggA})$, as well as different A boson widths Γ_A. The results of these fits are used to set constraints on the parameter space of the 2HDM. The background model is the same as for the $b\bar{b}A$ search.

The search for a Z' and W' boson seeks resonances in the mass range from 300 GeV to 5 TeV, while the search for a pseudoscalar seeks resonances in a mass range from 220 GeV to 2 TeV. In total, 19 simulated signal mass hypotheses are tested. In addition, parameter morphing [123] is applied to the shape and normalisation of the $m_{\text{T},Vh}$ and m_{Vh} distributions for all four signal hypotheses in order to interpolate between the simulated signal mass points.

The same normalisation factors are used across the various regions entering the likelihood fit. However, dedicated nuisance parameters exist to account for extrapolation effects between the signal and control regions, between the resolved and merged categories as well as between the different lepton channels. The corresponding extrapolation uncertainties are detailed in Table 4 and Table 5. The normalisation

scale factors and their uncertainties obtained from a background-only fit in the various signal and control regions of the combined 0- and 2-lepton channels, as well as the combined 0- and 1-lepton channels, are summarised in Table 6. In the search for the bbA process, separate normalisation scale factors are used for top + hf and top + lf production. Separate normalisation scale factors for top + lf are used for the 0-lepton and 2-lepton channels, while a common normalisation scale factor is used for top + hf due to statistical limitations in the 3+ b-tags regions of the 2-lepton channel. The normalisation scale factors are consistent with unity for top + lf and 1.27 ± 0.15 for top + hf. Since the top + hf process gives only small contributions to the 1 b-tag and 2 b-tag signal regions, no bias was found in the ggA, Z' and W' fit models, in which top + hf and top + lf are described by a common normalisation scale factor.

Table 6: Post-fit normalisation scale factors (NF) and their uncertainties obtained from a combined background-only fit to the various signal and control regions of the 0- and 2-lepton channels and from a combined background-only fit of the 0- and 1-lepton channels. Numbers are presented for the background components that are allowed to float in the likelihood fit. The top-quark background is normalised with separate NFs for the 0-, 1- and 2-lepton regions, while the NFs for the Z + hf and Z + hl backgrounds are correlated between the 0- and 2-lepton channels.

Background	0-lepton	2-lepton	1-lepton
Combined Z'/ggA fit of 0- and 2-lepton channels			
top	0.92 ± 0.05	1.02 ± 0.02	–
Z + hf	1.18 ± 0.07		–
Z + hl	1.16 ± 0.06		–
Combined W' fit of 0- and 1-lepton channels			
top	0.92 ± 0.04	–	0.93 ± 0.04
Z + hf	1.30 ± 0.16	–	–
Z + hl	1.30 ± 0.16	–	–
W + hf	–	–	1.35 ± 0.18
W + hl	–	–	1.34 ± 0.12
Combined $b\bar{b}A$ fit of 0- and 2-lepton channels			
top + hf	1.27 ± 0.15		–
top + lf	0.92 ± 0.11	1.03 ± 0.08	–
Z + jets ($N^{b\text{-tags}} \geq 3$)	1.19 ± 0.15		–
Z + hf	1.21 ± 0.07		–
Z + hl	1.12 ± 0.06		–

The $m_{\mathrm{T},Vh}$ and m_{Vh} distributions after a fit of the background templates to data are shown in Figures 3 and 4 for the signal regions used in the search for a Z' boson. Similar distributions are obtained from the 2HDM ggA fits, with background yields consistent within the uncertainties. Figure 5 shows the signal region distributions in the 1-lepton channel after the W' fit. The distributions of the $m_{\mathrm{T},Vh}$ and m_{Vh} observables are presented in Figure 6 for events with three or more b-tags (i.e. regions used in the search for the $b\bar{b}A$ process) after a fit of the background templates to data. Control region distributions are presented in Figure 7.

The expected and observed event yields after fits of the backgrounds as well as the $b\bar{b}A$ and W' signals to

data are shown in Table 7.

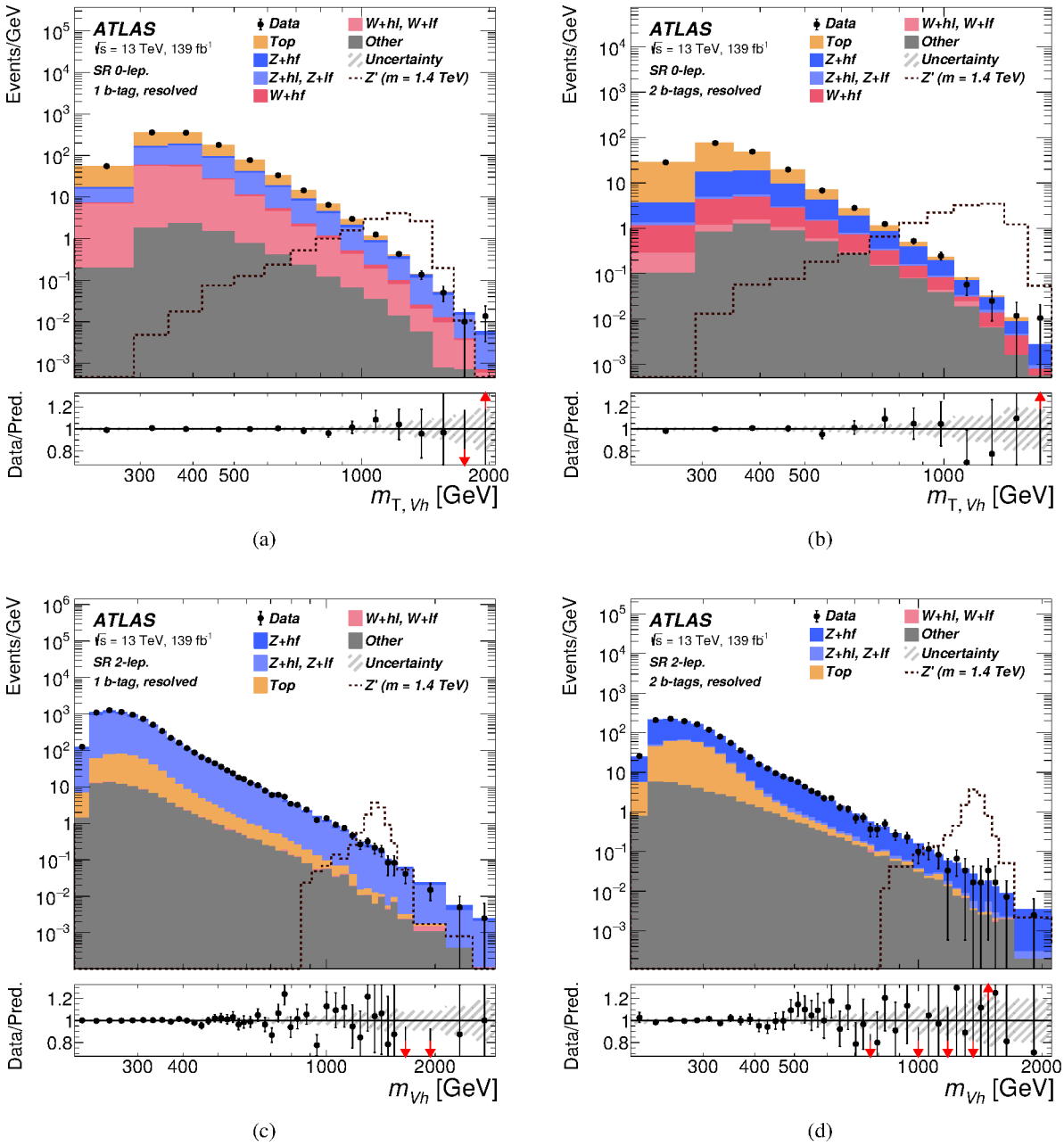

Figure 3: Event distributions of $m_{\mathrm{T},Vh}$ for the 0-lepton SR (a, b) and of m_{Vh} for the 2-lepton SR (c, d) in the resolved categories of the Z' fit. The quantity on the vertical axis is the number of data events divided by the bin width in GeV. The term 'Top' summarises events from $t\bar{t}$, single-top-quark, $t\bar{t}+h$ and $t\bar{t}+V$ contributions. In each plot, the last bin contains the overflow. The background prediction is shown after a background-only maximum-likelihood fit to the data. The lower panels show the ratio of the observed to the estimated SM background. The background uncertainty band shows the post-fit statistical and systematic components added in quadrature. The signal for the benchmark HVT *Model A* with $m_{Z'} = 1.4$ TeV, normalised to $\sigma \times B(Zh) \times B(h \to b\bar{b}) = 0.1$ pb, is shown as a dashed line.

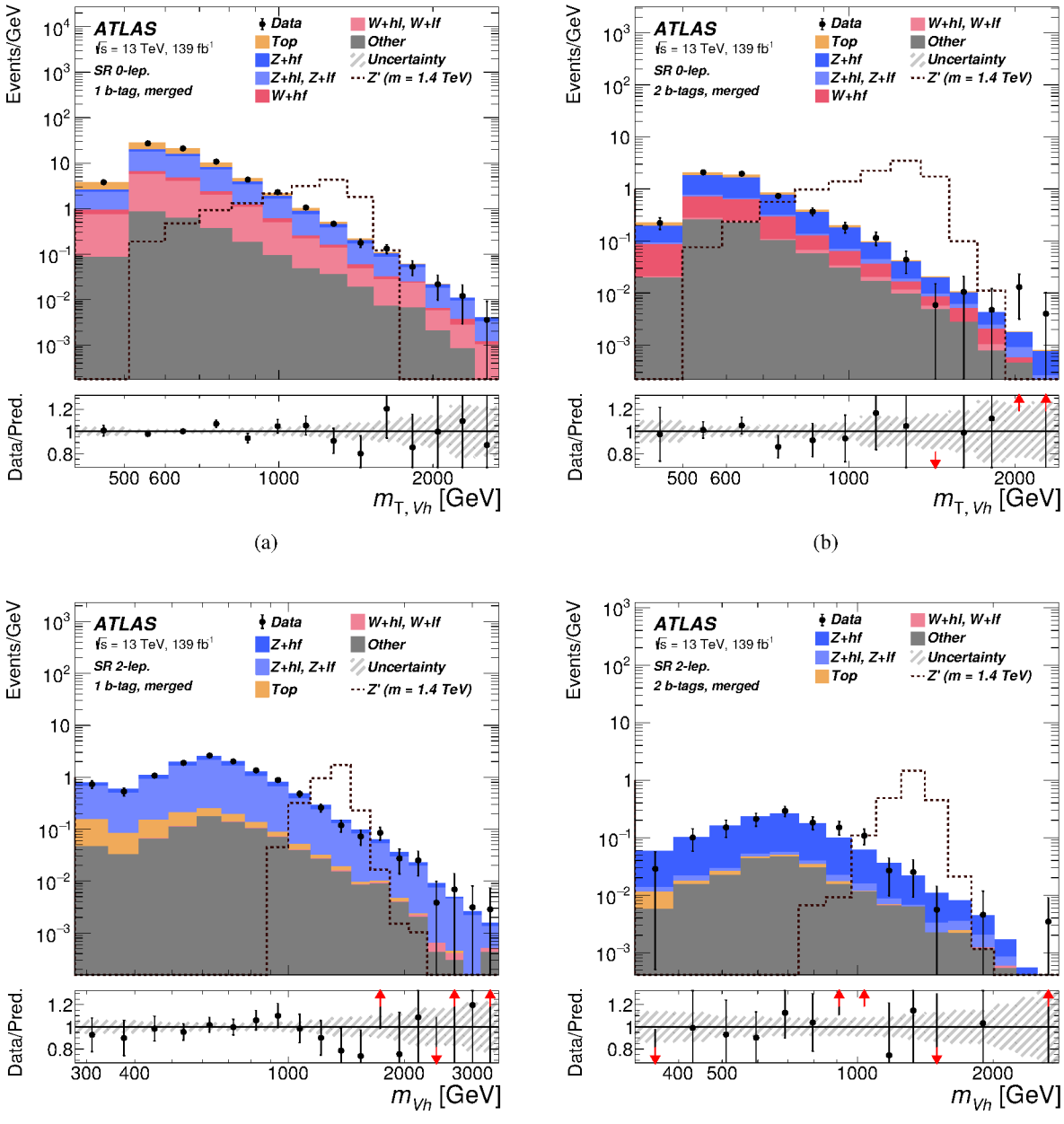

Figure 4: Event distributions of $m_{\mathrm{T},Vh}$ for the 0-lepton channel (a, b) and of m_{Vh} for the 2-lepton channels (c, d) in the merged categories of the Z' fit. The quantity on the vertical axis is the number of data events divided by the bin width in GeV. The term 'Top' summarises events from $t\bar{t}$, single-top-quark, $t\bar{t}+h$ and $t\bar{t}+V$ contributions. In each plot, the last bin contains the overflow. The background prediction is shown after a background-only maximum-likelihood fit to the data. The signal for the benchmark HVT *Model A* with $m_{Z'} = 1.4$ TeV, normalised to $\sigma \times B(Zh) \times B(h \to b\bar{b}) = 0.1$ pb, is shown as a dashed line. The lower panels show the ratio of the observed to the estimated SM background. The background uncertainty band shows the post-fit statistical and systematic components added in quadrature.

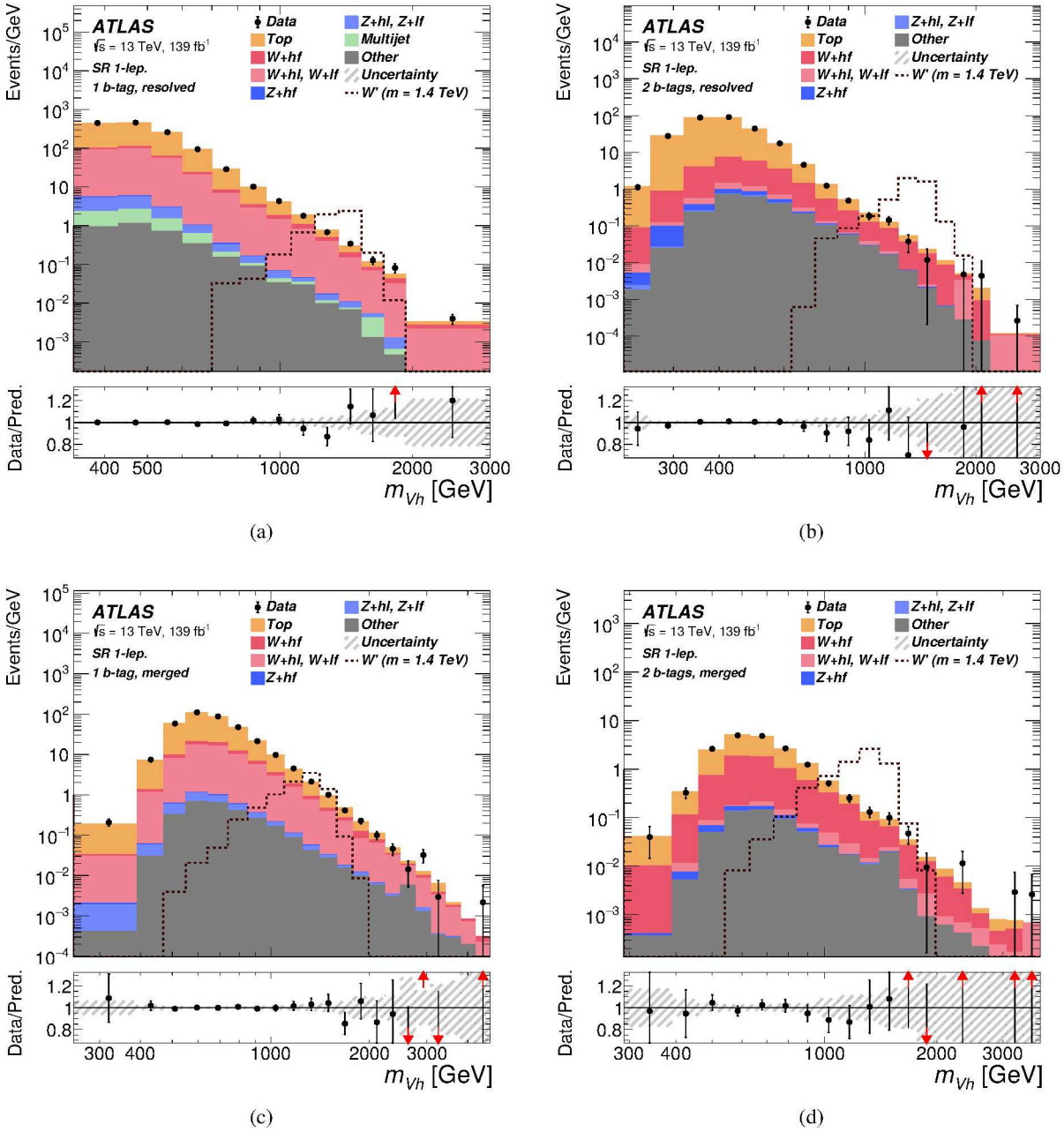

Figure 5: Event distributions of m_{Vh} for the 1-lepton SR in the resolved (a, b) and merged (c, d) categories of the W' fit. The quantity on the vertical axis is the number of data events divided by the bin width in GeV. The term 'Top' summarises events from $t\bar{t}$, single-top-quark, $t\bar{t}+h$ and $t\bar{t}+V$ contributions. In each plot, the last bin contains the overflow. The background prediction is shown after a background-only maximum-likelihood fit to the data. The lower panels show the ratio of the observed to the estimated SM background. The background uncertainty band shows the post-fit statistical and systematic uncertainties added in quadrature. The signal for the benchmark HVT *Model A* with $m_{W'} = 1.4$ TeV is shown as a dashed line and normalised to a cross section times branching fraction of 0.1 pb.

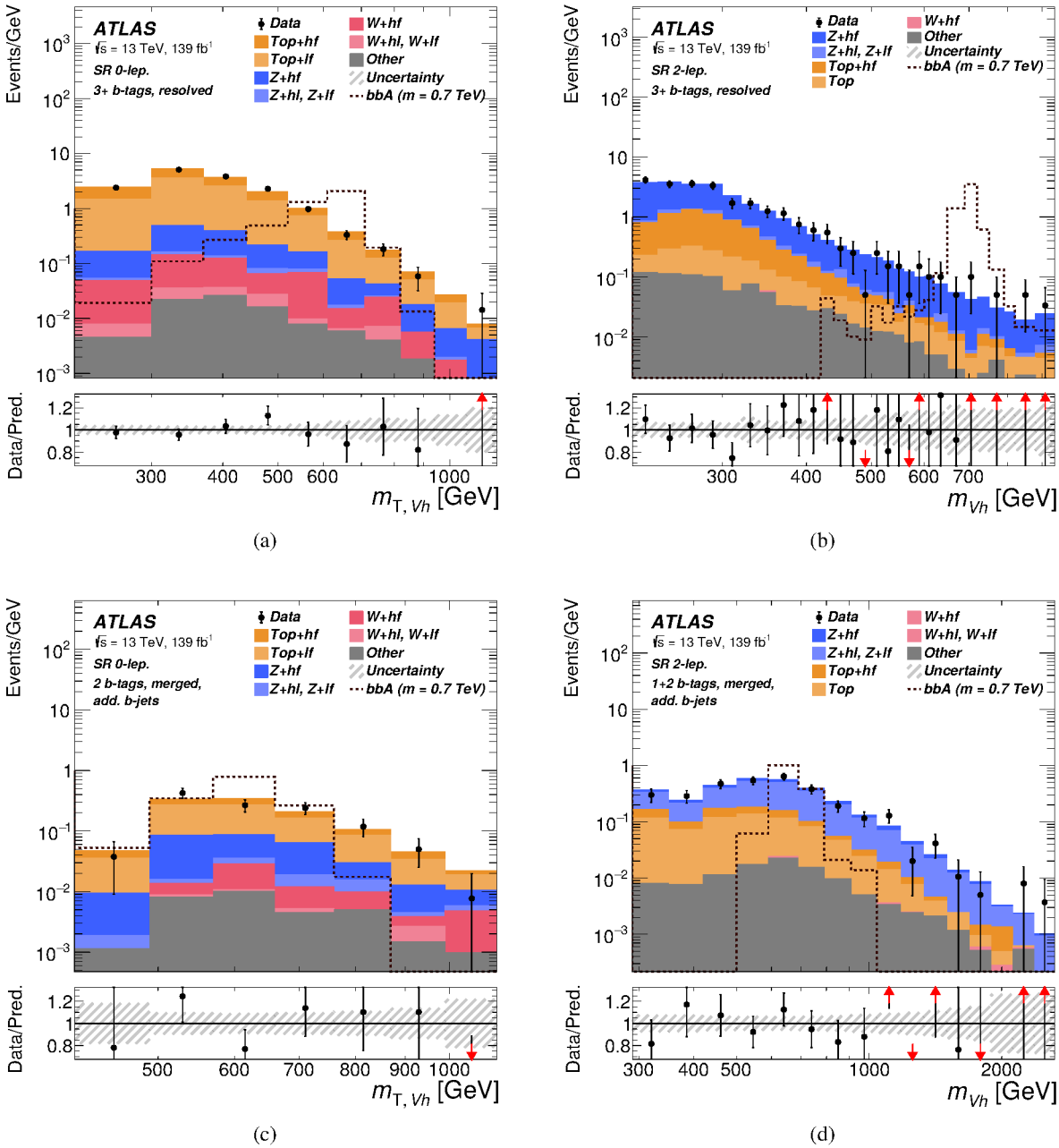

Figure 6: Event distributions of $m_{\mathrm{T},Vh}$ for the 0-lepton channel (a, c) and of m_{Vh} for the 2-lepton channels (b, d) in the merged and resolved 3+ tag SR categories of the $b\bar{b}A$ fit. The term 'Top' summarises events from $t\bar{t}$, single-top-quark, $t\bar{t}+h$ and $t\bar{t}+V$ contributions. The quantity on the vertical axis is the number of data events divided by the bin width in GeV. In each plot, the last bin contains the overflow. The background prediction is shown after a background-only maximum-likelihood fit to the data. The signal for the benchmark 2HDM model with $m_A = 0.7$ TeV, normalised to $\sigma \times B(Zh) \times B(h \to b\bar{b}) = 0.1$ pb, is shown as a dashed line. The lower panels show the ratio of the observed to the estimated SM background. The background uncertainty band shows the post-fit statistical and systematic components added in quadrature.

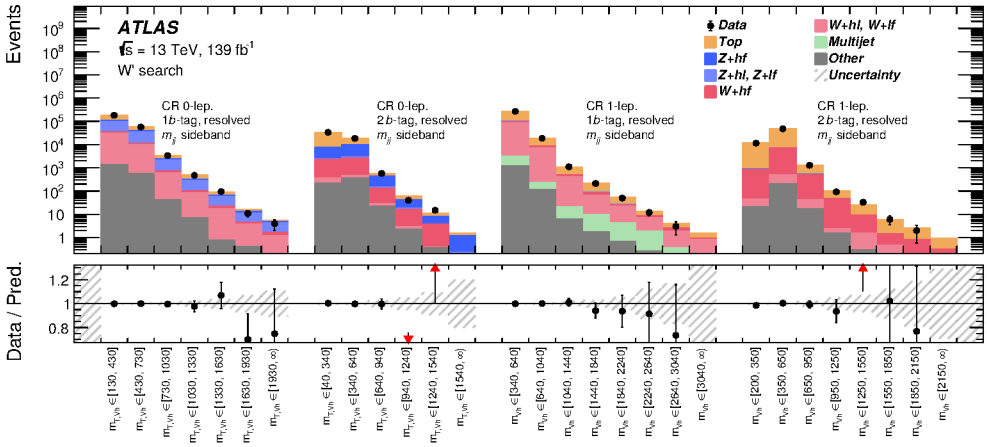

(a)

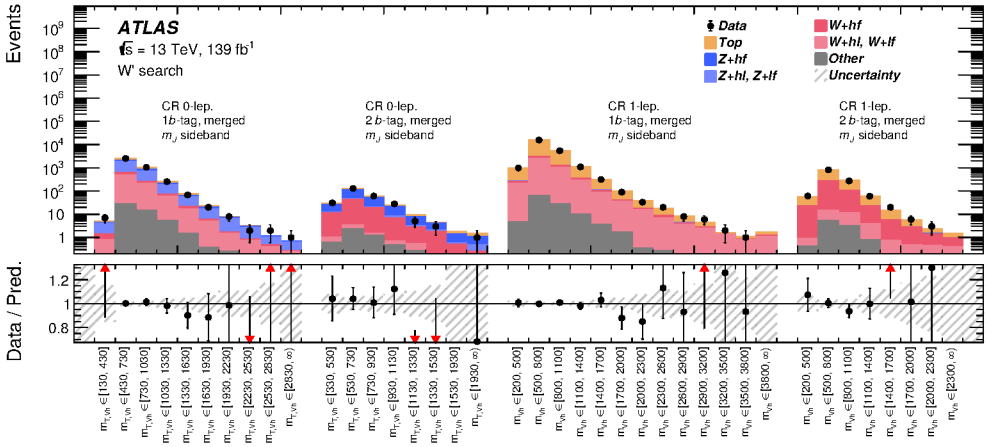

(b)

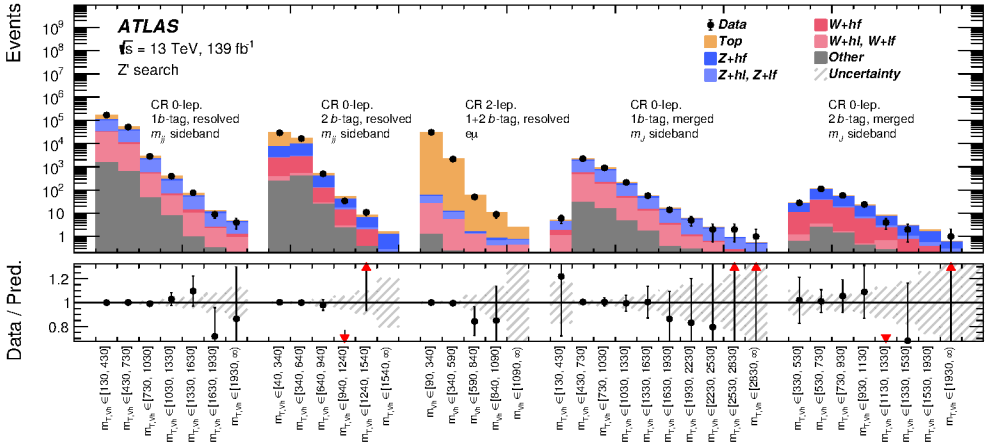

(c)

Figure 7: Distributions of the m_{Vh} and $m_{\mathrm{T},Vh}$ observables in the control regions of the (a) resolved and (b) merged event categories used for the W' search as well as (c) the control regions of the resolved and merged event categories used in the Z' search. The term 'Top' summarises events from $t\bar{t}$, single-top-quark, $t\bar{t}+h$ and $t\bar{t}+V$ contributions. The distributions are presented after a background-only maximum-likelihood to data. The lower panels show the ratio of the observed to the estimated SM background. The background uncertainty band shows the post-fit statistical and systematic uncertainties added in quadrature.

Table 7: The observed event yields and background predictions in the various signal regions after fitting a signal and the various background templates to the data. The yields in the 0- and 2-lepton channels correspond to the $b\bar{b}A$ fit for a signal of mass 420 GeV. The yields in the 1-lepton channel are derived from the W' fit for a signal of mass 1400 GeV. The term Top summarises events from $t\bar{t}$, single-top-quark, $t\bar{t}$ + h and $t\bar{t}$ +V contributions. The quoted uncertainties are the statistical and systematic uncertainties combined in quadrature after the fit. The uncertainties in the individual background predictions are larger than the total background uncertainty due to correlations between the normalisation parameters in the fit.

	Resolved			Merged		
0-lepton	*1 b-tag*	*2 b-tags*	*3+ b-tags*	*1 b-tag*	*2 b-tags*	*add. b-tags*
Top	40400 ± 600	10200 ± 200	1140 ± 31	2000 ± 100	71.9 ± 3.4	77 ± 5
Z + hf	3700 ± 100	3000 ± 100	82.1 ± 3.3	651 ± 32	298 ± 12	19.2 ± 1.4
Z + hl	20700 ± 400	106 ± 13	5.5 ± 0.8	2300 ± 100	12.9 ± 0.8	2.5 ± 0.2
Z + lf	1600 ± 200	5.0 ± 2.1	0.1 ± 0.1	396 ± 34	0.8 ± 0.3	< 0.1
W + hf	1140 ± 80	860 ± 60	30.9 ± 2.1	243 ± 24	106 ± 11	3.9 ± 0.6
W + hl	10000 ± 400	90 ± 10	3.6 ± 0.5	1100 ± 100	5.8 ± 0.6	0.4 ± 0.1
W + lf	1915 ± 270	13 ± 4.4	< 0.1	234 ± 31	0.5 ± 0.2	< 0.1
Diboson	470 ± 60	68 ± 8	3.8 ± 0.4	280 ± 40	78 ± 11	2.6 ± 0.3
SM Vh	223 ± 13	292 ± 16	3.7 ± 0.2	24.2 ± 1.7	15.2 ± 1.0	0.5 ± 0.1
Total	80100 ± 220	14650 ± 90	1266 ± 21	7260 ± 60	587 ± 13	106 ± 5
Data	80110	14681	1265	7260	584	105
2-lepton	*1 b-tag*	*2 b-tags*	*3+ b-tags*	*1 b-tag*	*2 b-tags*	*add. b-tags*
Top	8100 ± 200	6000 ± 200	135 ± 4	44.8 ± 3.0	2.8 ± 0.2	79.4 ± 4.8
Z + hf	23200 ± 500	17100 ± 100	327 ± 9	208 ± 7	98 ± 4	33.2 ± 2.2
Z + hl	102500 ± 1100	450 ± 40	16.9 ± 1.9	709 ± 15	4.6 ± 0.2	157 ± 7
Z + lf	6800 ± 1000	29 ± 11	< 0.1	154 ± 11	0.3 ± 0.1	18.1 ± 1.7
W + hf	4.9 ± 1.2	1.5 ± 0.1	< 0.1	0.2 ± 0.0	< 0.1	< 0.1
W + hl	25 ± 4	0.2 ± 0.1	< 0.1	1.3 ± 0.0	< 0.1	< 0.1
W + lf	0.7 ± 0.1	< 0.1	< 0.1	0.3 ± 0.0	< 0.1	< 0.1
Diboson	1660 ± 80	480 ± 20	13.1 ± 0.6	85.5 ± 3.0	20.5 ± 0.9	10.1 ± 0.4
SM Vh	333 ± 13	402 ± 11	5.1 ± 0.2	5.1 ± 0.2	2.6 ± 0.1	0.9 ± 0.1
Total	142700 ± 300	24400 ± 100	496 ± 11	1208 ± 16	129 ± 4	298 ± 7
Data	142672	24371	505	1220	133	311
1-lepton	*1 b-tag*	*2 b-tags*	*3+ b-tags*	*1 b-tag*	*2 b-tags*	*add. b-tags*
Top	86540 ± 470	18174 ± 88	–	26070 ± 200	1073 ± 23	–
Z + lf	108 ± 20	0.4 ± 0.1	–	22.6 ± 5.9	< 0.1	–
Z + hl	561 ± 83	5.2 ± 0.9	–	111 ± 14	0.9 ± 0.1	–
Z + hf	84 ± 20	59 ± 12	–	20.9 ± 4.5	10.9 ± 2.4	–
W + lf	2080 ± 230	0.7 ± 0.3	–	1011 ± 81	1.8 ± 0.5	–
W + hl	22330 ± 530	92.8 ± 6.6	–	5670 ± 180	21.1 ± 1.7	–
W + hf	2910 ± 110	1457 ± 54	–	1219 ± 38	60 ± 20	–
Diboson	160 ± 15	16.3 ± 1.4	–	251 ± 19	32.9 ± 2.7	–
SM Vh	150 ± 14	190 ± 17	–	32.6 ± 2.7	25.9 ± 2.2	–
Multijet	298 ± 58	< 0.1	–	< 0.1	< 0.1	–
Total	115210 ± 280	19995 ± 80	–	34410 ± 120	1769 ± 27	–
Data	115145	20017	–	34403	1771	–

The largest deviation from the Standard Model expectations is found in the Z' and ggA searches for a resonance mass of 500 GeV and corresponds to a local significance of about 2.1 standard deviations (and a p-value, i.e. the probability that the background can produce a fluctuation greater than the excess observed in data, of 0.017). The global significance of this excess corresponds to 1.1 standard deviations. The $b\bar{b}A$ search displays a similar excess of 1.6 standard deviations (p-value of 0.059) around the same resonance mass. For all three fit models, the excess originates mainly from the 2 b-tag category of the 2-lepton channel, where small differences between the observations and SM predictions are found for m_{Vh} values around 500 GeV. The local significance in the $b\bar{b}A$ search is lower than in the $Z'$and ggA searches because the additional signal regions used in the search for the $b\bar{b}A$ process do not display any excess. Another excess is found in the Z' search at a resonance mass of 2.2 TeV and corresponds to a local significance of about 2.0 standard deviations (p-value of 0.02). The W' search finds mild excesses at resonance masses of 400 GeV (about 2.0 standard deviations, p-value of 0.02) and 3.0 TeV (about 1.7 standard deviations, p-value of 0.05).

The 95% CL upper limits on the production cross section for $Z' \to Zh$ are shown in Figure 8(a) as a function of the resonance mass. The observed limits range from 0.9 pb for $m_{Z'} = 300$ GeV to 0.3 fb for $m_{Z'} = 5$ TeV. These limits exclude Z' masses below 2.8 TeV for HVT benchmark *Model A* with coupling constant $g_V = 1$ [12]. For *Model B* with coupling constant $g_V = 3$ [12], Z' masses below 3.2 TeV are excluded. The combined limits are dominated by the 0-lepton (2-lepton) channel for resonance masses above (below) 800 GeV. The limits on the $m_{Z'} = 5$ TeV signal hypothesis were also calculated using pseudo-experiments to validate the asymptotic approximation approach in a phase-space region strongly limited by a low number of data events. It was found that the two statistical methods agree within 20%.

The dominant uncertainties for low resonance masses (i.e. $m_{Z'} = 500$ GeV) are due to the modelling of the parton shower in $t\bar{t}$ background events and to the QCD scale uncertainties in the Z + hf background. At intermediate resonance masses (i.e. $m_{Z'} = 800$ GeV), the large-R jet mass resolution uncertainties become increasingly important and so do the uncertainties related to the matching of the matrix element to the parton shower for the various W+ jets background contributions. The latter uncertainties are also the dominant systematic uncertainties for Z' resonance masses above 2 TeV. The statistical uncertainties of the data become dominant for resonance masses above 600 GeV.

Figure 8(b) shows the 95% CL upper limits on the production cross section for $W' \to Wh$ as a function of the resonance mass. The limits range from 1.3 pb for $m_{W'} = 400$ GeV to 0.4 fb for $m_{W'} = 5$ TeV. These limits exclude W' masses below 2.95 TeV for HVT benchmark *Model A* with coupling constant $g_V = 1$ [12]. For *Model B* with coupling constant $g_V = 3$, W' masses below 3.3 TeV are excluded. The combined limits are dominated by the 1-lepton channel over the full range of tested mass hypotheses. The limits on the $m_{W'} = 5$ TeV signal hypothesis were also calculated using pseudo-experiments to validate the asymptotic approximation approach in a phase-space region strongly limited by a low number of data events. It was found that the two statistical methods agree within 10%.

Figure 9(a) shows the 95% CL upper limits on the production cross section of ggA multiplied by its branching fraction to Zh as a function of the resonance mass. The observed limits range from 0.6 pb for $m_A = 220$ GeV to 3 fb for $m_A = 2$ TeV. Figure 9(b) shows the 95% CL upper limits on the production cross section of $b\bar{b}A$ multiplied by its branching fraction to Zh as a function of the resonance mass. The observed limits range from 0.5 pb for $m_A = 220$ GeV to 2.5 fb for $m_A = 2$ TeV.

The upper limits on the production cross section times branching ratio obtained from the Z' and W' searches

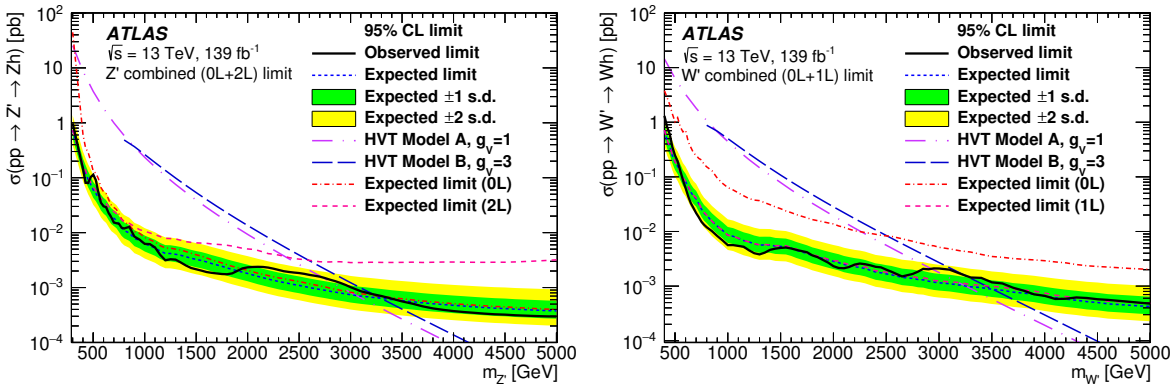

(a) (b)

Figure 8: Upper limits at the 95% CL on the product of the cross section for $pp \to Z'$ and the branching fraction to Zh from the combination of the 0-lepton (0L) and 2-lepton (2L) channels (a) and on the product of the cross section for $pp \to W'$ and the branching fraction to Wh from the combination of the 0-lepton and 1-lepton (1L) channels (b). For the Z' and W' search, the branching fraction of $h \to b\bar{b}, c\bar{c}$ is assumed to be 0.598.

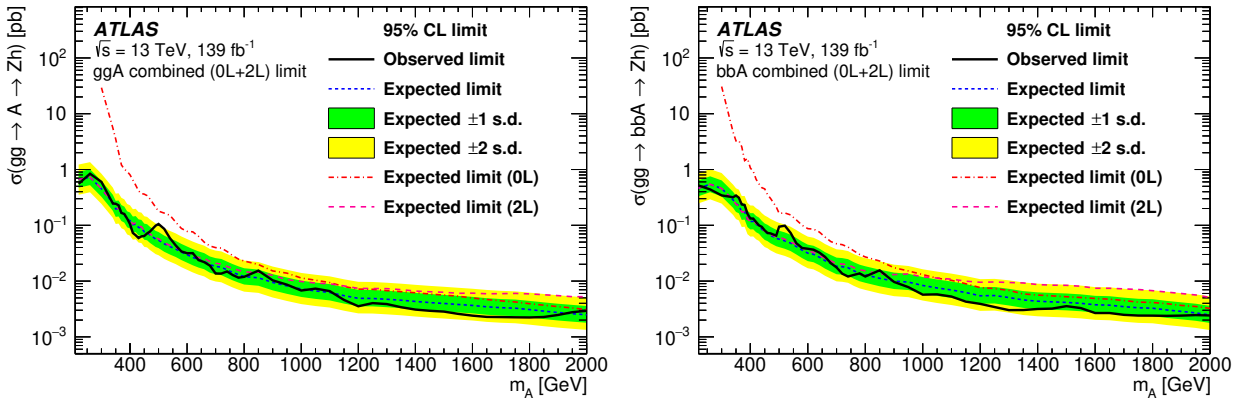

(a) (b)

Figure 9: Upper limits at the 95% CL on the product of the cross section for (a) $gg \to A$ and (b) $b\bar{b} \to A$ and their respective branching fraction to Zh from the combination of the 0-lepton (0L) and 2-lepton (2L) channels. For the $gg \to A$ search, the possible signal components of the data are interpreted assuming pure gluon–gluon fusion production. For both searches, a branching fraction of 0.569 for $h \to b\bar{b}$ [124] is assumed.

are used to set 95% CL exclusion contours in the HVT parameter plane $\{g_F, g_H\}$[8] [125]. Exclusion contours are shown in Figure 10 for resonance masses of 2, 3 and 4 TeV. The constraints on g_F and g_H are stronger for large coupling parameter values and become weaker as these coupling parameters approach zero. This is because the resonance couplings to Vh vanish as the g_H parameter reaches zero, while for $g_F = 0$ the Z' and W' production cross sections in the quark–antiquark annihilation mode become zero.

Figure 11 shows the expected and observed two-dimensional likelihood scans of the b-associated production cross section times branching fraction $B(A \to Zh)$ versus the gluon–gluon fusion production cross section

[8] The coupling constants g_H and g_F are related to those in Ref. [12] as follows: the Higgs boson coupling is $g_H = g_V c_H$ and the universal fermion coupling is $g_F = g^2 c_F / g_V$, where g is the SM $SU(2)_L$ gauge coupling.

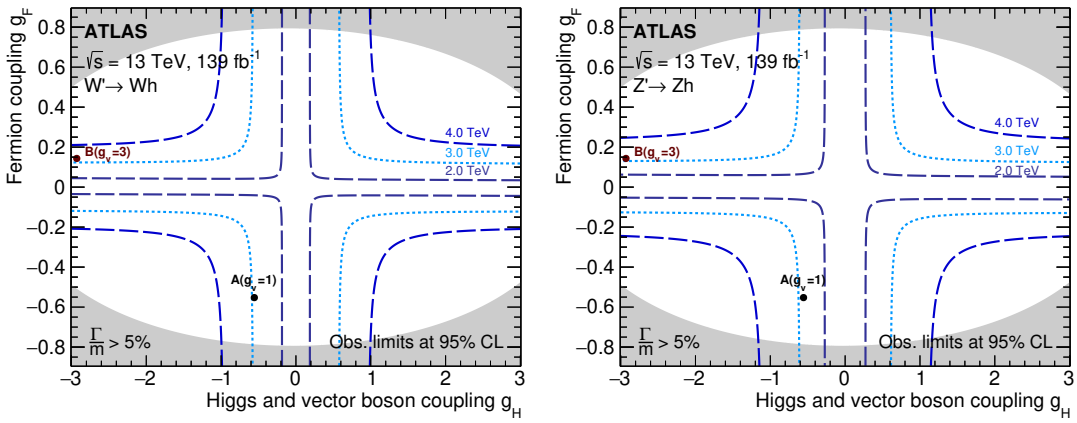

Figure 10: Observed limits on the HVT model at 95% CL in the g_F vs g_H plane for resonance masses of 2, 3 and 4 TeV in the Wh channel (left) and in the Zh channel (right). The circles indicate the coupling values for models A and B and the grey region corresponds to the area of phase space where the decay width of the resonance is no longer negligible and the signal m_{Vh} shape is no longer expected to be dominated by the experimental resolution.

times branching fraction $B(A \to Zh)$ for various pseudoscalar masses m_A. For each mass hypothesis, the best-fit value is compatible with the absence of a signal. The largest difference between the observed and expected best-fit values is found for a resonance mass of $m_A = 500$ GeV.

To obtain the 95% CL upper limits on the 2HDM parameters, 95% CL upper limits on the production cross section for $A \to Zh$ are calculated for admixtures of ggA and $b\bar{b}A$ production modes and variations of the A boson natural width up to $\Gamma_A/m_A = 20\%$. For this interpretation, $m_{\mathrm{T},Vh}$ and m_{Vh} distributions of the simulated signal events are smeared according to a Breit–Wigner function with the width predicted by the parameters of the model. It was verified that this procedure produces line-shapes that are the same as those predicted by simulation.

Figure 12 shows the interpretation of the limits on ggA and $b\bar{b}A$ production in the Type-I, Type-II, Lepton-specific and Flipped 2HDM scenarios as a function of the parameters $\tan\beta$ and $\cos(\beta-\alpha)$ for $m_A = 700$ GeV. In the Type-I and Lepton-specific 2HDM models, a pseudoscalar with mass $m_A = 700$ GeV is excluded at the 95% CL for $\tan\beta$ values as large as 10. Greater sensitivity is observed at high $\tan\beta$ for the Type-II and Flipped models, due to a larger cross section for b-quark associated production. In the alignment limit $\cos(\beta-\alpha) \to 0$, the $A \to Zh$ branching fraction vanishes, thus the relatively low sensitivity around $\cos(\beta-\alpha) \approx 0$. Nevertheless, $\cos(\beta-\alpha)$ values down to around 0.07 can be excluded for all tested model scenarios. The narrow inclined regions with no sensitivity at low $\tan\beta$ are caused by a vanishing $h \to bb$ branching fraction.

Figure 13 shows the interpretation of the cross-section limits as a function of the parameters $\tan\beta$ and m_A for $\cos(\beta-\alpha) = 0.1$. The shape of the expected exclusions is determined by the interplay of the expected cross-section limit, which decreases as a function of m_A, and the signal production cross section times the $A \to Zh$ branching fraction at given m_A and $\tan\beta$ values. This branching fraction decreases significantly at $m_A = 350$ GeV because the $A \to t\bar{t}$ decay becomes possible, but increases again at higher m_A values. The parameter $\tan\beta$ controls the admixture of the gluon–gluon fusion and b-quark associated production, and thus affects the rate at which the signal cross section falls as a function of m_A, leading to a varying sensitivity as a function of $\tan\beta$. The excesses or deficits in the data visible in Figure 9 are also reflected in Figure 13.

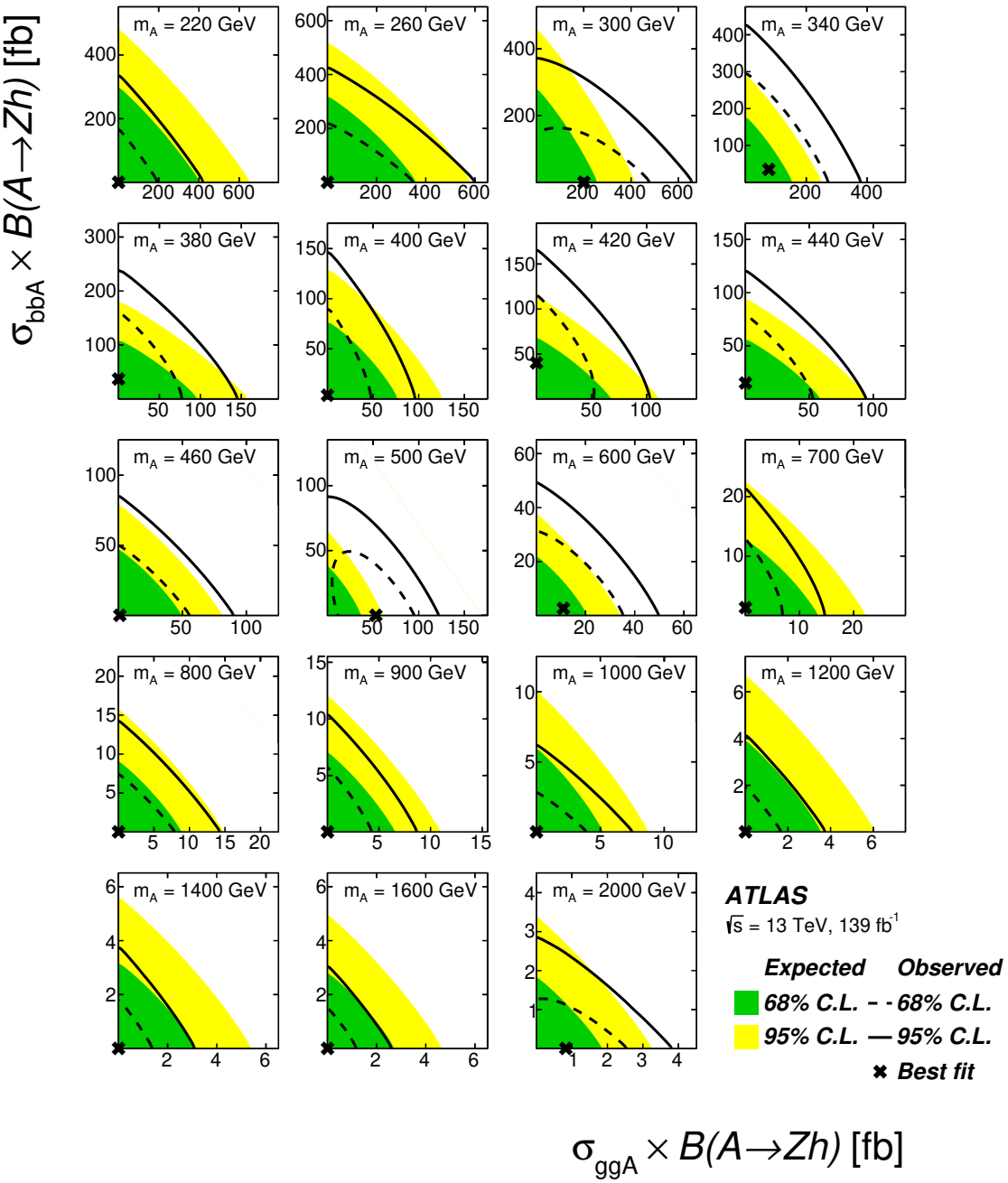

Figure 11: Expected and observed two-dimensional likelihood scans of the b-associated production cross section times branching fraction, $\sigma_{b\bar{b}A} \times B(A \to Zh)$, vs the gluon–gluon fusion cross section times branching fraction, $\sigma_{ggA} \times B(A \to Zh)$, for a given A boson mass (m_A). For each mass, a variety of different cross-section hypotheses are scanned. At each point, 2Δ(NLL) is calculated, defined as the negative-log-likelihood (NLL) of the conditional fit to the Asimov and observed datasets with $\sigma_{b\bar{b}A}$ and σ_{ggA} fixed to their values at that point and with the minimum NLL value at any point subtracted. The best-fit point and the preferred 68% and 95% CL boundaries are found at 2Δ(NLL) values of 0.0, 2.30 and 5.99, respectively.

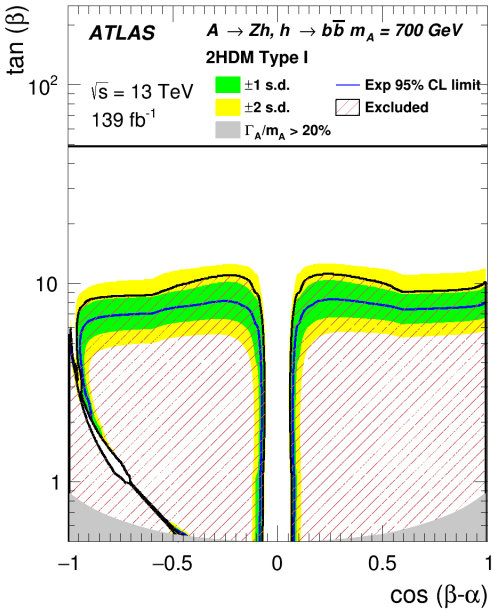

(a) 2HDM Type-I

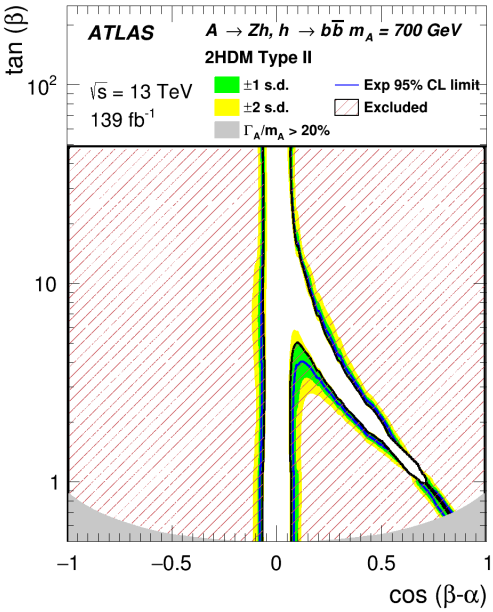

(b) 2HDM Type-II

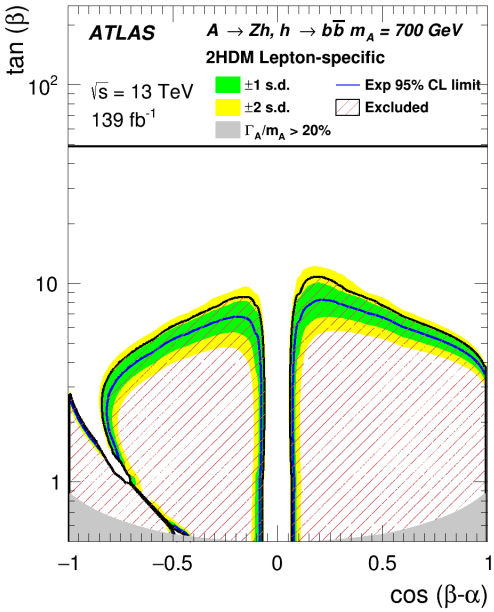

(c) 2HDM Lepton-specific

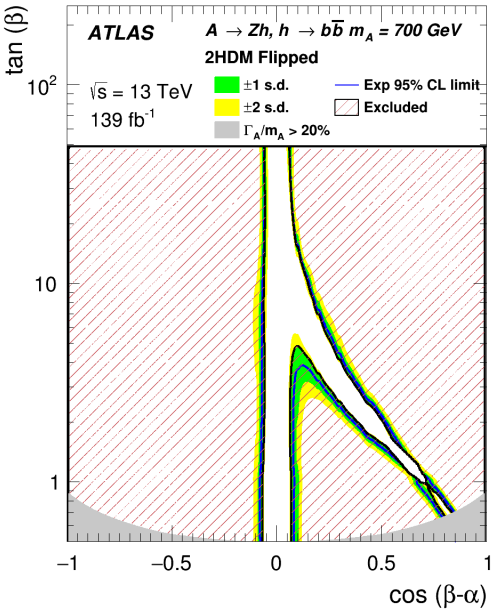

(d) 2HDM Flipped

Figure 12: The interpretation of the cross-section limits in the context of the various 2HDM types as a function of the parameters $\tan\beta$ and $\cos(\beta-\alpha)$ for $m_A = 700$ GeV: (a) Type-I , (b) Type-II, (c) Lepton-specific, and (d) Flipped. Variations of the natural width up to $\Gamma_A/m_A = 20\%$ have been taken into account. For the interpretation in Type-II and Flipped 2HDM, the b-quark associated production is included in addition to the gluon–gluon fusion production. The exclusion limits are only evaluated for $\tan\beta < 50$ because larger $\tan\beta$ values are disfavoured by most models (and cross-section predictions become less reliable).

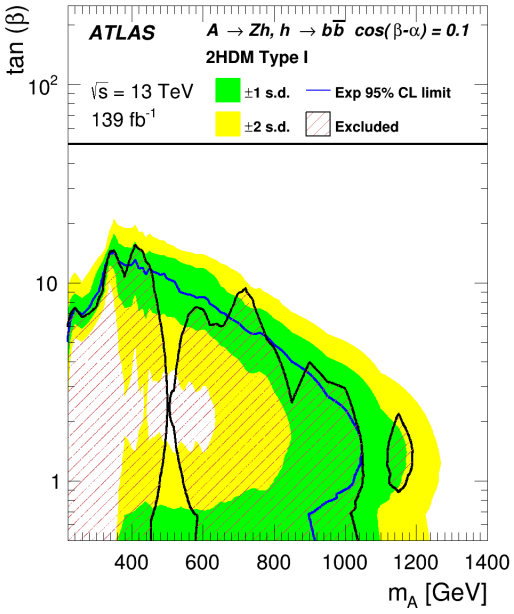

(a) 2HDM Type-I

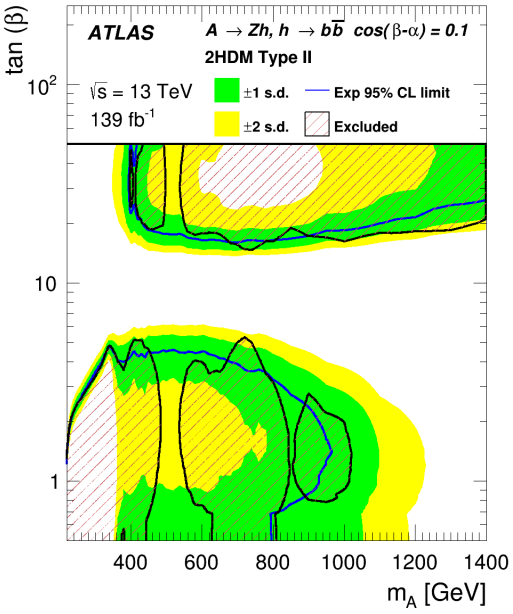

(b) 2HDM Type-II

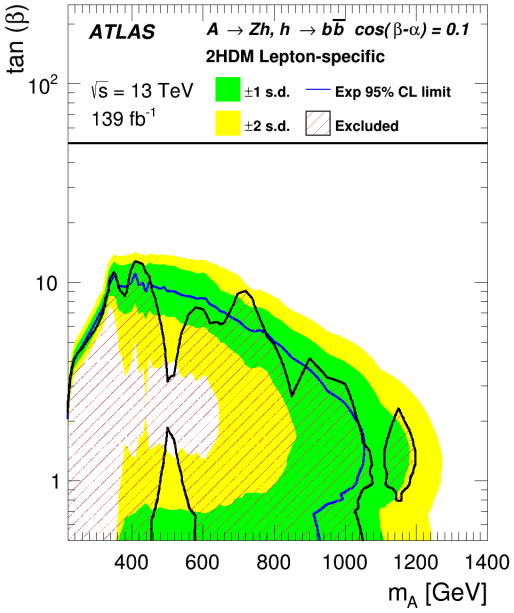

(c) 2HDM Lepton-specific

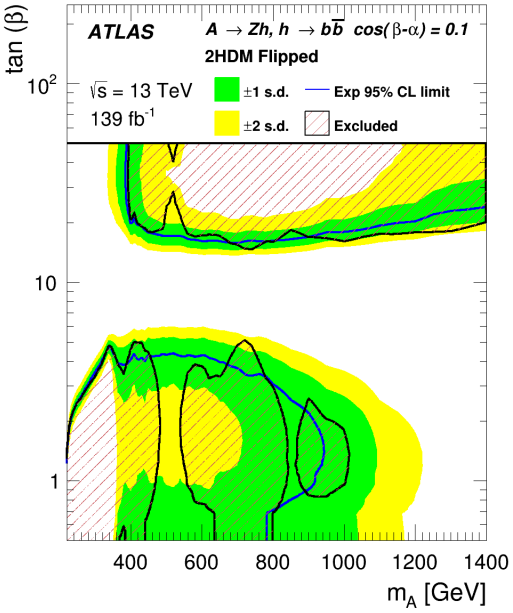

(d) 2HDM Flipped

Figure 13: The interpretation of the cross-section limits in the context of the various 2HDM types as a function of the parameters $\tan\beta$ and m_A for $\cos(\beta-\alpha) = 0.1$: (a) Type-I , (b) Type-II, (c) Lepton-specific, and (d) Flipped. Variations of the natural width up to $\Gamma_A/m_A = 20\%$ have been taken into account. The exclusion limits are only evaluated for $\tan\beta < 50$ because larger $\tan\beta$ values are disfavoured by most models (and cross-section predictions become less reliable).

9 Conclusion

A search for Z' and W' bosons and for a CP-odd Higgs boson A in the $\nu\bar{\nu}b\bar{b}$, $\ell^+\ell^- b\bar{b}$ and $\ell^\pm \nu b\bar{b}$ final states is performed using 139 fb^{-1} of 13 TeV pp collision data collected with the ATLAS detector at the LHC. No significant excess of events is observed above the SM predictions in the three channels, and upper limits are set on the respective production cross sections.

The 95% CL upper limits on the production cross section for $Z' \to Zh$ range from 0.9 pb for $m_{Z'} = 300$ GeV to 0.3 fb for $m_{Z'} = 5$ TeV. These limits exclude Z' masses below 2.8 TeV for HVT benchmark *Model A* with coupling constant $g_V = 1$. For *Model B* with coupling constant $g_V = 3$, Z' masses below 3.2 TeV are excluded. The Z' cross-section limits are also converted into constraints on the couplings in the g_F vs g_H plane for resonance mass hypotheses of 2, 3 and 4 TeV.

The 95% CL upper limits on the production cross section for $W' \to Wh$ range from around 1.3 pb for $m_{W'} = 400$ GeV to 0.4 fb for $m_{W'} = 5$ TeV. These limits exclude W' masses below 2.95 TeV for HVT benchmark *Model A* with coupling constant $g_V = 1$. For *Model B* with coupling constant $g_V = 3$, W' masses below 3.3 TeV are excluded. The W' cross-section limits are also converted into constraints on the couplings in the g_F vs g_H plane for resonance mass hypotheses of 2, 3 and 4 TeV.

The 95% CL upper limits on the cross section for ggA production multiplied by the A boson's branching fraction to Zh range from 0.6 pb for $m_A = 220$ GeV to 3 fb for $m_A = 2$ TeV. The 95% CL upper limits on the cross section for $b\bar{b}A$ production multiplied by the A boson's branching fraction to Zh range from 0.5 pb for $m_A = 220$ GeV to 2.5 fb for $m_A = 2$ TeV. The limits on the ggA and $b\bar{b}A$ production cross sections are converted into constraints on the parameters $\tan\beta$, $\cos(\beta - \alpha)$ and m_A in the Type-I, Type-II, Lepton-specific and Flipped 2HDM scenarios.

The cross-section limits improve on the results from the ATLAS analysis of the partial Run 2 dataset. The improvements range from about 50% for a resonance mass of 220 GeV to about 400% for a mass of 5 TeV. The improvements at low resonance masses are mainly due to the larger dataset, while at high resonance masses the improvements are mostly due to refined b-tagging techniques, including the use of variable-radius track-jets instead of track-jets clustered with a fixed radius parameter of $R = 0.2$.

References

[1] ATLAS Collaboration, *Observation of a new particle in the search for the Standard Model Higgs boson with the ATLAS detector at the LHC*, Phys. Lett. B **716** (2012) 1, arXiv: 1207.7214 [hep-ex].

[2] CMS Collaboration, *Observation of a new boson at a mass of 125 GeV with the CMS experiment at the LHC*, Phys. Lett. B **716** (2012) 30, arXiv: 1207.7235 [hep-ex].

[3] S. Weinberg, *Gauge hierarchies*, Phys. Lett. B **82** (1979) 387.

[4] M. J. G. Veltman, *The infrared - ultraviolet connection*, Acta Phys. Polon. B **12** (1981) 437.

[5] S. Llewellyn et al., *The real gauge hierarchy problem*, Phys. Lett. B **105** (1981) 38.

[6] F. Sannino et al., *Orientifold theory dynamics and symmetry breaking*, Phys. Rev. D **71** (2005) 051901, arXiv: hep-ph/0405209 [hep-ph].

[7] R. Foadi et al., *Minimal walking technicolor: Setup for collider physics*, Phys. Rev. D **76** (2007) 055005, arXiv: 0706.1696 [hep-ph].

[8] A. Belyaev et al., *Technicolor walks at the LHC*, Phys. Rev. D **79** (2009) 035006, arXiv: 0809.0793 [hep-ph].

[9] M. Schmaltz et al., *LITTLE HIGGS THEORIES*, Ann. Rev. Nucl. Part. Sci. **55** (2005) 229, arXiv: hep-ph/0502182 [hep-ph].

[10] M. J. Dugan et al., *Anatomy of a composite Higgs model*, Nucl. Phys. B **254** (1985) 299.

[11] K. Agashe et al., *The minimal composite Higgs model*, Nucl. Phys. B **719** (2005) 165, arXiv: hep-ph/0412089 [hep-ph].

[12] D. Pappadopulo et al., *Heavy vector triplets: bridging theory and data*, JHEP **09** (2014) 060, arXiv: 1402.4431 [hep-ph].

[13] J. de Blas et al., *Combining searches of Z' and W' bosons*, JHEP **01** (2013) 166, arXiv: 1211.2229 [hep-ph].

[14] G. C. Branco et al., *Theory and phenomenology of two-Higgs-doublet models*, Phys. Rept. **516** (2012) 1, arXiv: 1106.0034 [hep-ph].

[15] P. Fayet, *Supersymmetry and weak, electromagnetic and strong interactions*, Phys. Lett. B **64** (1976) 159.

[16] P. Fayet, *Spontaneously broken supersymmetric theories of weak, electromagnetic and strong interactions*, Phys. Lett. B **69** (1977) 489.

[17] G. R. Farrar et al., *Phenomenology of the production, decay, and detection of new hadronic states associated with supersymmetry*, Phys. Lett. B **76** (1978) 575.

[18] P. Fayet, *Relations between the masses of the superpartners of leptons and quarks, the goldstino couplings and the neutral currents*, Phys. Lett. B **84** (1979) 416.

[19] H. Georgi et al., *Softly Broken Supersymmetry and SU(5)*, Nucl. Phys. B **193** (1981) 150.

[20] J. E. Kim, *Light pseudoscalars, particle physics and cosmology*, Phys. Rept. **150** (1987) 1.

[21] M. Joyce et al., *Nonlocal electroweak baryogenesis. II. The classical regime*, Phys. Rev. D **53** (1996) 2958, arXiv: hep-ph/9410282 [hep-ph].

[22] ATLAS Collaboration, *Search for heavy resonances decaying into a W or Z boson and a Higgs boson in final states with leptons and b-jets in 36 fb^{-1} of $\sqrt{s}$ = 13 TeV pp collisions with the ATLAS detector*, JHEP **03** (2018) 174, arXiv: 1712.06518 [hep-ex], Erratum: JHEP **11** (2018) 051.

[23] CMS Collaboration, *Search for heavy resonances decaying to WW, WZ, or WH boson pairs in a final state consisting of a lepton and a large-radius jet in proton-proton collisions at $\sqrt{s}$ = 13 TeV*, Phys. Rev. D **105** (2022) 032008, arXiv: 2109.06055 [hep-ex].

[24] CMS Collaboration, *Search for a heavy vector resonance decaying to a Z boson and a Higgs boson in proton-proton collisions at $\sqrt{s}$ = 13 TeV*, Eur. Phys. J. C **81** (2021) 688, arXiv: 2102.08198 [hep-ex].

[25] ATLAS Collaboration, *Search for resonances decaying into a weak vector boson and a Higgs boson in the fully hadronic final state produced in proton–proton collisions at $\sqrt{s}$ = 13 TeV with the ATLAS detector*, Phys. Rev. D **102** (2020) 112008, arXiv: 2007.05293 [hep-ex].

[26] CMS Collaboration, *Search for heavy resonances that decay into a vector boson and a Higgs boson in hadronic final states at $\sqrt{s}$ = 13 TeV*, Eur. Phys. J. C **77** (2017) 636, arXiv: 1707.01303 [hep-ex].

[27] CMS Collaboration, *Search for a heavy pseudoscalar Higgs boson decaying into a 125 GeV Higgs boson and a Z boson in final states with two tau and two light leptons at $\sqrt{s}$ = 13 TeV*, JHEP **03** (2020) 065, arXiv: 1910.11634 [hep-ex].

[28] V. D. Barger et al., *Gauge model with light W and Z bosons*, Phys. Rev. D **22** (1980) 727.

[29] R. Contino et al., *On the effect of resonances in composite Higgs phenomenology*, JHEP **10** (2011) 081, arXiv: 1109.1570 [hep-ph].

[30] ATLAS Collaboration, *The ATLAS Experiment at the CERN Large Hadron Collider*, JINST **3** (2008) S08003.

[31] ATLAS Collaboration, *The ATLAS Collaboration Software and Firmware*, ATL-SOFT-PUB-2021-001, 2021, URL: https://cds.cern.ch/record/2767187.

[32] ATLAS Collaboration, *Luminosity determination in pp collisions at $\sqrt{s}$ = 8 TeV using the ATLAS detector at the LHC*, Eur. Phys. J. C **76** (2016) 653, arXiv: 1608.03953 [hep-ex].

[33] ATLAS Collaboration, *ATLAS data quality operations and performance for 2015–2018 data-taking*, JINST **15** (2020) P04003, arXiv: 1911.04632 [physics.ins-det].

[34] S. Frixione et al., *The automated computation of tree-level and next-to-leading order differential cross sections, and their matching to parton shower simulations*, JHEP **07** (2014) 079, arXiv: 1405.0301 [hep-ph].

[35] T. Sjöstrand et al., *A brief introduction to PYTHIA 8.1*, Comput. Phys. Commun. **178** (2008) 852, arXiv: 0710.3820 [hep-ph].

[36] ATLAS Collaboration, *ATLAS Pythia 8 tunes to 7 TeV data*, ATL-PHYS-PUB-2014-021, 2014, URL: https://cds.cern.ch/record/1966419.

[37] R. D. Ball et al., *Impact of heavy quark masses on parton distributions and LHC phenomenology*, Nucl. Phys. B **849** (2011) 296, arXiv: 1101.1300 [hep-ph].

[38] E. Bothmann et al., *Event Generation with Sherpa 2.2*, SciPost Phys. **7** (2019) 034, arXiv: 1905.09127 [hep-ph].

[39] NNPDF Collaboration, *Parton distributions for the LHC run II*, JHEP **04** (2015) 040, arXiv: 1410.8849 [hep-ph].

[40] T. Gleisberg et al., *Comix, a new matrix element generator*, JHEP **12** (2008) 039, arXiv: 0808.3674 [hep-ph].

[41] F. Buccioni et al., *OpenLoops 2*, Eur. Phys. J. C **79** (2019) 866, arXiv: 1907.13071 [hep-ph].

[42] F. Cascioli et al., *Scattering Amplitudes with Open Loops*, Phys. Rev. Lett. **108** (2012) 111601, arXiv: 1111.5206 [hep-ph].

[43] A. Denner et al., *Collier: A fortran-based complex one-loop library in extended regularizations*, Comput. Phys. Commun. **212** (2017) 220, arXiv: 1604.06792 [hep-ph].

[44] S. Schumann et al., *A Parton shower algorithm based on Catani-Seymour dipole factorisation*, JHEP **03** (2008) 038, arXiv: 0709.1027 [hep-ph].

[45] S. Höche et al., *A critical appraisal of NLO+PS matching methods*, JHEP **09** (2012) 049, arXiv: 1111.1220 [hep-ph].

[46] F Siegert et al., *QCD matrix elements + parton showers. The NLO case*, JHEP **04** (2013) 027, arXiv: 1207.5030 [hep-ph].

[47] S. Catani et al., *QCD Matrix Elements + Parton Showers*, JHEP **11** (2001) 063, arXiv: hep-ph/0109231.

[48] S. Höche et al., *QCD matrix elements and truncated showers*, JHEP **05** (2009) 053, arXiv: 0903.1219 [hep-ph].

[49] C. Anastasiou et al., *High-precision QCD at hadron colliders: Electroweak gauge boson rapidity distributions at next-to-next-to leading order*, Phys. Rev. D **69** (2004) 094008, arXiv: hep-ph/0312266.

[50] S. Frixione et al., *A positive-weight next-to-leading-order Monte Carlo for heavy flavour hadroproduction*, JHEP **09** (2007) 126, arXiv: 0707.3088 [hep-ph].

[51] P. Nason, *A new method for combining NLO QCD with shower Monte Carlo algorithms*, JHEP **11** (2004) 040, arXiv: hep-ph/0409146.

[52] S. Frixione et al., *Matching NLO QCD computations with Parton Shower simulations: the POWHEG method*, JHEP **11** (2007) 070, arXiv: 0709.2092 [hep-ph].

[53] S. Alioli et al., *A general framework for implementing NLO calculations in shower Monte Carlo programs: the POWHEG BOX*, JHEP **06** (2010) 043, arXiv: 1002.2581 [hep-ph].

[54] T. Sjöstrand et al., *An introduction to PYTHIA 8.2*, Comput. Phys. Commun. **191** (2015) 159, arXiv: 1410.3012 [hep-ph].

[55] ATLAS Collaboration, *Studies on top-quark Monte Carlo modelling for Top2016*, ATL-PHYS-PUB-2016-020, 2016, URL: https://cds.cern.ch/record/2216168.

[56] M. Beneke et al., *Hadronic top-quark pair production with NNLL threshold resummation*, Nucl. Phys. B **855** (2012) 695, arXiv: 1109.1536 [hep-ph].

[57] M. Cacciari et al., *Top-pair production at hadron colliders with next-to-next-to-leading logarithmic soft-gluon resummation*, Phys. Lett. B **710** (2012) 612, arXiv: 1111.5869 [hep-ph].

[58] P. Bärnreuther et al., *Percent-Level-Precision Physics at the Tevatron: Next-to-Next-to-Leading Order QCD Corrections to $q\bar{q} \to t\bar{t} + X$*, Phys. Rev. Lett. **109** (2012) 132001, arXiv: 1204.5201 [hep-ph].

[59] M. Czakon et al., *NNLO corrections to top-pair production at hadron colliders: the all-fermionic scattering channels*, JHEP **12** (2012) 054, arXiv: 1207.0236 [hep-ph].

[60] M. Czakon et al., *NNLO corrections to top pair production at hadron colliders: the quark-gluon reaction*, JHEP **01** (2013) 080, arXiv: 1210.6832 [hep-ph].

[61] M. Czakon et al., *Total Top-Quark Pair-Production Cross Section at Hadron Colliders Through $O(\alpha_S^4)$*, Phys. Rev. Lett. **110** (2013) 252004, arXiv: 1303.6254 [hep-ph].

[62] M. Czakon et al., *Top++: A Program for the Calculation of the Top-Pair Cross-Section at Hadron Colliders*, Comput. Phys. Commun. **185** (2014) 2930, arXiv: 1112.5675 [hep-ph].

[63] S. Frixione et al., *Single-top hadroproduction in association with a W boson*, JHEP **07** (2008) 029, arXiv: 0805.3067 [hep-ph].

[64] ATLAS Collaboration, *Multi-Boson Simulation for 13 TeV ATLAS Analyses*, ATL-PHYS-PUB-2017-005, 2017, URL: https://cds.cern.ch/record/2261933.

[65] J. Butterworth et al., *PDF4LHC recommendations for LHC Run II*, J. Phys. G **43** (2016) 023001, arXiv: 1510.03865 [hep-ph].

[66] ATLAS Collaboration, *Measurement of the Z/γ^* boson transverse momentum distribution in pp collisions at $\sqrt{s} = 7$ TeV with the ATLAS detector*, JHEP **09** (2014) 145, arXiv: 1406.3660 [hep-ex].

[67] R. Harlander et al., *Soft gluon resummation for gluon-induced Higgs Strahlung*, JHEP **11** (2014) 082, arXiv: 1410.0217 [hep-ph].

[68] ATLAS Collaboration, *The Pythia 8 A3 tune description of ATLAS minimum bias and inelastic measurements incorporating the Donnachie–Landshoff diffractive model*, ATL-PHYS-PUB-2016-017, 2016, URL: https://cds.cern.ch/record/2206965.

[69] D. J. Lange, *The EvtGen particle decay simulation package*, Nucl. Instrum. Meth. A **462** (2001) 152.

[70] ATLAS Collaboration, *The ATLAS Simulation Infrastructure*, Eur. Phys. J. C **70** (2010) 823, arXiv: 1005.4568 [physics.ins-det].

[71] GEANT4 Collaboration, *GEANT4 a simulation toolkit*, Nucl. Instrum. Meth. A **506** (2003) 250.

[72] ATLAS Collaboration, *Vertex Reconstruction Performance of the ATLAS Detector at $\sqrt{s} = 13$ TeV*, ATL-PHYS-PUB-2015-026, 2015, URL: https://cds.cern.ch/record/2037717.

[73] ATLAS Collaboration, *Electron and photon performance measurements with the ATLAS detector using the 2015-2017 LHC proton-proton collision data*, JINST **14** (2019) P12006, arXiv: 1908.00005 [hep-ex].

[74] ATLAS Collaboration, *Muon reconstruction and identification efficiency in ATLAS using the full Run 2 pp collision data set at $\sqrt{s} = 13$ TeV*, Eur. Phys. J. C **81** (2021) 578, arXiv: 2012.00578 [hep-ex].

[75] G. Salam et al., *The anti-k_t jet clustering algorithm*, JHEP **04** (2008) 063, arXiv: 0802.1189 [hep-ph].

[76] M. Cacciari et al., *FastJet User Manual*, Eur. Phys. J. C **72** (2012) 1896, arXiv: 1111.6097 [hep-ph].

[77] ATLAS Collaboration, *Topological cell clustering in the ATLAS calorimeters and its performance in LHC Run 1*, Eur. Phys. J. C **77** (2017) 490, arXiv: 1603.02934 [hep-ex].

[78] W. Lampl et al., *Calorimeter Clustering Algorithms: Description and Performance*, ATL-LARG-PUB-2008-002, 2008, URL: https://cds.cern.ch/record/1099735.

[79] ATLAS Collaboration, *Performance of pile-up mitigation techniques for jets in pp collisions at $\sqrt{s} = 8$ TeV using the ATLAS detector*, Eur. Phys. J. C **76** (2016) 581, arXiv: 1510.03823 [hep-ex].

[80] ATLAS Collaboration, *Improving jet substructure performance in ATLAS using Track-CaloClusters*, tech. rep. ATL-PHYS-PUB-2017-015, CERN, 2017, URL: https://cds.cern.ch/record/2275636.

[81] D. Krohn et al., *Jet trimming*, JHEP **02** (2010) 084, arXiv: 0912.1342 [hep-ph].

[82] S. Catani et al., *Longitudinally-invariant $k_\perp$-clustering algorithms for hadron-hadron collisions*, Nucl. Phys. B **406** (1993) 187.

[83] S. D. Ellis et al., *Successive combination jet algorithm for hadron collisions*, Phys. Rev. D **48** (1993) 3160, arXiv: hep-ph/9305266.

[84] ATLAS Collaboration, *Identification of Boosted, Hadronically-Decaying W and Z Bosons in $\sqrt{s} = 13$ TeV Monte Carlo Simulations for ATLAS*, ATL-PHYS-PUB-2015-033, 2015, URL: https://cds.cern.ch/record/2041461.

[85] ATLAS Collaboration, *Jet energy scale measurements and their systematic uncertainties in proton–proton collisions at $\sqrt{s}$ = 13 TeV with the ATLAS detector*, Phys. Rev. D **96** (2017) 072002, arXiv: 1703.09665 [hep-ex].

[86] ATLAS Collaboration, *Jet energy resolution in proton–proton collisions at $\sqrt{s}$ = 7 TeV recorded in 2010 with the ATLAS detector*, Eur. Phys. J. C **73** (2013) 2306, arXiv: 1210.6210 [hep-ex].

[87] ATLAS Collaboration, *Variable Radius, Exclusive-k_T, and Center-of-Mass Subjet Reconstruction for Higgs($\to b\bar{b}$) Tagging in ATLAS*, tech. rep. ATL-PHYS-PUB-2017-010, CERN, 2017, URL: https://cds.cern.ch/record/2268678.

[88] ATLAS Collaboration, *Identification of boosted Higgs bosons decaying into b-quark pairs with the ATLAS detector at 13 TeV*, Eur. Phys. J. C **79** (2019) 836, arXiv: 1906.11005 [hep-ex].

[89] ATLAS Collaboration, *ATLAS b-jet identification performance and efficiency measurement with $t\bar{t}$ events in pp collisions at $\sqrt{s}$ = 13 TeV*, Eur. Phys. J. C **79** (2019) 970, arXiv: 1907.05120 [hep-ex].

[90] ATLAS Collaboration, *Optimisation and performance studies of the ATLAS b-tagging algorithms for the 2017-18 LHC run*, ATL-PHYS-PUB-2017-013, 2017, URL: https://cds.cern.ch/record/2273281.

[91] ATLAS Collaboration, *Measurement of b-tagging efficiency of c-jets in $t\bar{t}$ events using a likelihood approach with the ATLAS detector*, ATLAS-CONF-2018-001, 2018, URL: https://cds.cern.ch/record/2306649.

[92] ATLAS Collaboration, *Calibration of light-flavour b-jet mistagging rates using ATLAS proton–proton collision data at $\sqrt{s}$ = 13 TeV*, ATLAS-CONF-2018-006, 2018, URL: https://cds.cern.ch/record/2314418.

[93] ATLAS Collaboration, *Identification and energy calibration of hadronically decaying tau leptons with the ATLAS experiment in pp collisions at $\sqrt{s}$=8 TeV*, Eur. Phys. J. C **75** (2015) 303, arXiv: 1412.7086 [hep-ex].

[94] ATLAS Collaboration, *Reconstruction of hadronic decay products of tau leptons with the ATLAS experiment*, Eur. Phys. J. C **76** (2016) 295, arXiv: 1512.05955 [hep-ex].

[95] ATLAS Collaboration, *Performance of missing transverse momentum reconstruction with the ATLAS detector using proton–proton collisions at $\sqrt{s}$ = 13 TeV*, Eur. Phys. J. C **78** (2018) 903, arXiv: 1802.08168 [hep-ex].

[96] ATLAS Collaboration, *E_T^{miss} performance in the ATLAS detector using 2015–2016 LHC pp collisions*, ATLAS-CONF-2018-023, 2018, URL: https://cds.cern.ch/record/2625233.

[97] ATLAS Collaboration, *Object-based missing transverse momentum significance in the ATLAS Detector*, ATLAS-CONF-2018-038, 2018, URL: https://cds.cern.ch/record/2630948.

[98] ATLAS Collaboration, *Measurements of WH and ZH production in the $H \to b\bar{b}$ decay channel in pp collisions at 13 TeV with the ATLAS detector*, Eur. Phys. J. C **81** (2021) 178, arXiv: 2007.02873 [hep-ex].

[99] ATLAS Collaboration, *Performance of the missing transverse momentum triggers for the ATLAS detector during Run-2 data taking*, JHEP **08** (2020) 080, arXiv: 2005.09554 [hep-ex].

[100] ATLAS Collaboration, *Observation of $H \to b\bar{b}$ decays and VH production with the ATLAS detector*, Phys. Lett. B **786** (2018) 59, arXiv: 1808.08238 [hep-ex].

[101] ATLAS Collaboration, *Performance of electron and photon triggers in ATLAS during LHC Run 2*, Eur. Phys. J. C **80** (2020) 47, arXiv: 1909.00761 [hep-ex].

[102] ATLAS Collaboration, *Performance of the ATLAS muon triggers in Run 2*, JINST **15** (2020) P09015, arXiv: 2004.13447 [hep-ex].

[103] ATLAS Collaboration, *Search for the standard model Higgs boson produced in association with top quarks and decaying into a $b\bar{b}$ pair in pp collisions at $\sqrt{s}$ = 13 TeV with the ATLAS detector*, Phys. Rev. D **97** (2018) 072016, arXiv: 1712.08895 [hep-ex].

[104] ATLAS Collaboration, *Jet mass reconstruction with the ATLAS Detector in early Run 2 data*, ATLAS-CONF-2016-035, 2016, URL: https://cds.cern.ch/record/2200211.

[105] ATLAS Collaboration, *Muon reconstruction performance of the ATLAS detector in proton–proton collision data at $\sqrt{s}$ = 13 TeV*, Eur. Phys. J. C **76** (2016) 292, arXiv: 1603.05598 [hep-ex].

[106] ATLAS Collaboration, *Electron reconstruction and identification in the ATLAS experiment using the 2015 and 2016 LHC proton–proton collision data at $\sqrt{s}$ = 13 TeV*, Eur. Phys. J. C **79** (2019) 639, arXiv: 1902.04655 [hep-ex].

[107] ATLAS Collaboration, *Reconstruction, Energy Calibration, and Identification of Hadronically Decaying Tau Leptons in the ATLAS Experiment for Run-2 of the LHC*, ATL-PHYS-PUB-2015-045, 2015, URL: https://cds.cern.ch/record/2064383.

[108] ATLAS Collaboration, *Luminosity determination in pp collisions at $\sqrt{s}$ = 13 TeV using the ATLAS detector at the LHC*, ATLAS-CONF-2019-021, 2019, URL: https://cds.cern.ch/record/2677054.

[109] G. Avoni et al., *The new LUCID-2 detector for luminosity measurement and monitoring in ATLAS*, JINST **13** (2018) P07017.

[110] A. D. Martin et al., *Parton distributions for the LHC*, Eur. Phys. J. C **63** (2009) 189, arXiv: 0901.0002 [hep-ph].

[111] J. Gao et al., *CT10 next-to-next-to-leading order global analysis of QCD*, Phys. Rev. D **89** (2014) 033009, arXiv: 1302.6246 [hep-ph].

[112] J. Bellm et al., *Herwig 7.0/Herwig++ 3.0 release note*, Eur. Phys. J. C **76** (2016) 196, arXiv: 1512.01178 [hep-ph].

[113] T. Sjöstrand et al., *A brief introduction to PYTHIA 8.1*, Comput. Phys. Commun. **178** (2008) 852, arXiv: 0710.3820 [hep-ph].

[114] L. Lönnblad, *Correcting the Colour-Dipole Cascade Model with Fixed Order Matrix Elements*, JHEP **05** (2002) 046, arXiv: hep-ph/0112284.

[115] L. Lönnblad et al., *Matching tree-level matrix elements with interleaved showers*, JHEP **03** (2012) 019, arXiv: 1109.4829 [hep-ph].

[116] I. Stewart et al., *Theory uncertainties for Higgs mass and other searches using jet bins*, Phys. Rev. D **85** (2012) 034011.

[117] J. M. Campbell et al., *MCFM for the Tevatron and the LHC*, Nucl. Phys. Proc. Suppl. (2010) 205, arXiv: 1007.3492 [hep-ph].

[118] L. Moneta et al., *The RooStats project*, 2010, arXiv: 1009.1003 [hep-ph].

[119] W. Verkerke et al., *The RooFit toolkit for data modeling*, 2003, arXiv: physics/0306116 [physics.data-an].

[120] M. Baak et al., *HistFitter software framework for statistical data analysis*, Eur. Phys. J. C **75** (2015) 153, arXiv: 1410.1280 [hep-ex].

[121] G. Cowan et al., *Asymptotic formulae for likelihood-based tests of new physics*, Eur. Phys. J. C **71** (2011) 1554, [Erratum: Eur. Phys. J. C **73** (2013) 2501], arXiv: 1007.1727 [physics.data-an].

[122] A. L. Read, *Presentation of search results: The CL_s technique*, J. Phys. G **28** (2002) 2693.

[123] M. Baak et al., *Interpolation between multi-dimensional histograms using a new non-linear moment morphing method*, Nucl. Instrum. Meth. A **771** (2015) 39, arXiv: 1410.7388 [physics.data-an].

[124] LHC Higgs Cross Section Working Group, *Handbook of LHC Higgs Cross Sections: 4. Deciphering the Nature of the Higgs Sector*, (2016), arXiv: 1610.07922 [hep-ph].

[125] ATLAS Collaboration, *Combination of searches for heavy resonances decaying into bosonic and leptonic final states using* 36 fb^{-1} *of proton-proton collision data at* $\sqrt{s} = 13$ TeV *with the ATLAS detector*, Phys. Rev. D **98** (2018) 052008.